11

APPLICATIONS OF MODERN DENSITY FUNCTIONAL THEORY TO SURFACES AND INTERFACES

G. PILANIA, H. ZHU, AND R. RAMPRASAD

11.1 INTRODUCTION

A surface or an interface provides a doorway through which any solid contacts and interacts with the external atmosphere or a second solid phase. At a fundamental level, surfaces and interfaces present model systems in which physics in two dimensions can be investigated and chemistry of bond breaking and bond formation between dissimilar systems can be studied [1, 2]. Understanding of surfaces and interfaces has not only extended our knowledge of basic physical and chemical sciences but also played key roles in the successful realization of many industrial processes [3–5]. For instance, surfaces form the basis of heterogeneous catalysis without which the present day chemical industry would not exist (at least the way we know it). Surface and interface science phenomena are pervasive in situations involving superlattices, crystal growth control, corrosion abatement, and nanostructured systems (where the surface or interface to volume ratio is large). Owing to its interdisciplinary nature, surface/interface science derives frequent contributions from physical, chemical, and materials sciences.

Density functional theory (DFT) based computations have been used for more than two decades in the arena of surface/interface science [6]. Several success stories of DFT in surface science are already well documented and hence are not repeated here. Famous examples such as the correct prediction of the

A Matter of Density: Exploring the Electron Density Concept in the Chemical, Biological, and Materials Sciences, First Edition. Edited by N. Sukumar.

Si(001)-(2 × 1) [7–12] and Si(111)-(7 × 7) [13, 14] reconstructed surfaces are now part of standard textbooks in the field [15]. DFT-based methods have not only evolved into an important tool for analyzing surface geometries and surface phases at various temperature, pressure, and chemical environments but also been applied successfully to model real-life heterogeneous surface catalysis [16, 17]. There are numerous examples in which DFT calculations have preceded experimental observations (see e.g., Reference 18). A more recent development that has contributed to the bridging of the experiment-theory gap is first principles thermodynamics (FPT) [19–21] which, as we discuss in detail later, involves a seamless combination of zero-temperature DFT results with statistical mechanics to provide pressure- and temperature-dependent observable properties that can be directly compared with experiments.

This chapter attempts to provide examples of some recent contributions made in the arena of surface/interface science using state-of-the-art DFT-based computations. While this is by no means a comprehensive account (and is highly colored by the authors' work and perspectives), materials systems and methodologies spanning several application areas including catalysis, crystal growth, and electronics are explored. Methodological details are provided where appropriate, and several references are provided when the scope and length of this presentation precludes a lengthy exposition of basic concepts.

11.2 THE PREDICTIVE CAPABILITY OF DFT

Among all modern electronic structure methods, DFT [22–26] is seen to offer the best trade-off between computational cost and accuracy. These methods are also referred to as "first-principles" or "ab initio" techniques to emphasize that there are no system-specific fitted parameters utilized during the course of such calculations. DFT has developed into a popular approach for predicting various structural and electronic properties of a wide range of materials systems including molecules, bulk solids, surfaces, and other low-dimensional nanostructures. In this section, we summarize the level of accuracy that one may expect from DFT calculations for some of the more basic properties before we plunge into surface/interface-based discussions.

Within Kohn–Sham DFT [22, 23], the following eigenvalue equation (in atomic units) is solved:

$$[-\nabla^2 + V_{\text{eff}}(r)]\Psi_i(r) = \epsilon_i \Psi_i(r), \tag{11.1}$$

where the first term in brackets represents the electronic kinetic energy (with ∇ being the gradient operator) and the second term, $V_{\text{eff}}(r)$, represents the effective potential energy seen by an electron. $V_{\text{eff}}(r)$ contains all the electron–electron and electron–nuclear interactions, as well as the potential caused by an external

electric field. In practice, the quantum mechanical part of the electron–electron interaction is approximated using (semi)local functionals such as the local density approximation (LDA) or generalized gradient approximations (GGA), or nonlocal hybrid functionals. $\Psi_i(r)$ and ϵ_i represent the spectrum of Kohn–Sham orbital wave functions and orbital energies, respectively, indexed by i. We note that for any given set of atomic positions (i.e., for given $V_{\text{eff}}(r)$), the above equation is solved self-consistently to result in converged charge densities (obtained from the wave functions of the occupied states), total energies (obtained from the wave functions and eigenenergies of the occupied states), and atomic forces (obtained from the first derivative of the total energy with respect to the position of any given atom). The atomic coordinates are optimized by the requirement that the total energy of the system is a minimum and that the forces on each atom are close to zero. Once the geometry is converged, several other properties of interest may be computed (as described in the rest of this chapter).

Some comments concerning the expected accuracy of DFT predictions are in order. The greatest strength of DFT is its ability to predict structural details of materials, typically to within 1% of experimental values. Figure 11.1 shows the correlation between DFT predictions of structural properties and experimental data for several classes of systems. Vibrational frequencies of molecules, phonon frequencies of solids, elastic constants of solids, and relative energies are predicted to within 2% of experiments by DFT. Figure 11.2a compares DFT predictions of vibrational frequencies of diatomic molecules with experiments, and Figure 11.2b shows a similar comparison for bulk and shear moduli for various solids. Dielectric constants of insulators are typically predicted to within 5% of experiments, as portrayed in Figure 11.2c for both static and optical dielectric constants. The larger discrepancy in this case is primarily caused by the lack of sufficiently accurate single-crystal experimental data.

The greatest deficiency of DFT is its inability to predict band gaps in semiconductors and insulators to the same level of accuracy achievable in the case of the other properties; DFT band gaps are underestimated relative to experimental determinations by up to 50%, as shown in Figure 11.2d. However, the shape and the width of the bands, and trends in changes in the band gap (e.g., due to external pressure), are predicted accurately [35]. The above deficiencies are the consequences of the approximations made within DFT such as the LDA or GGA, which include spurious electron self-interaction effects. Techniques to handle such deficiencies are currently available and include the use of hybrid functionals that are rising in popularity [36] and quasiparticle *GW* (note that GW is not an acronym; here G and W represent the Green function and screened coulomb interaction, respectively) corrections to the electronic energy levels (References 34 and 37). Such treatments, although computationally more expensive than conventional DFT, result in satisfactory agreement of the computed band gaps with experiments as shown in Figure 11.2d for the case of *GW* corrections.

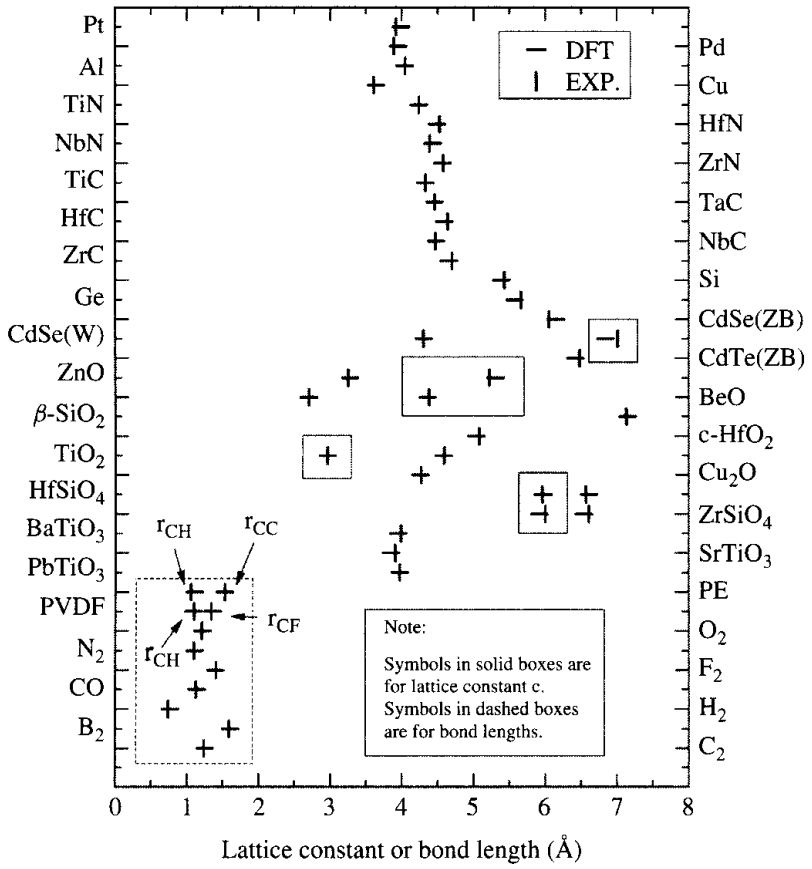

Figure 11.1 Comparison of DFT-computed structural parameters with experiments for a variety of metals, semiconductors, insulators, polymers, and molecules. ZB and W represent the zinc blende and wurtzite crystal structures, respectively. Data are from various sources [27–30]. (Reprinted with permission from R. Ramprasad, N. Shi, and C. Tang. Modeling the physics and chemistry of interfaces in nanodielectrics. In Dielectric Polymer Nanocomposites. J. K. Nelson (Ed.), Springer (2010). Copyright 2010 by Springer.)

11.3 SLAB MODELS USED IN SURFACE/INTERFACE STUDIES

At a surface/interface, periodicity and translational symmetry of a bulk crystal are destroyed. Atoms at these boundaries possess broken bonds and reduced or altered coordination as compared to their bulk counterparts. To simulate a surface/interface, either one has to specifically apply two-dimensional periodic boundary conditions, or one could impose three-dimensional periodic boundary conditions along with incorporation of a vacuum region normal to the surface/interface. The latter approach, referred to as *the slab supercell model*, is more commonly used (as many DFT codes implicitly involve three-dimensional periodic boundary conditions). The supercell, when repeated in all three dimensions, gives rise to a series of stacked slabs of the material separated by vacuum spaces.

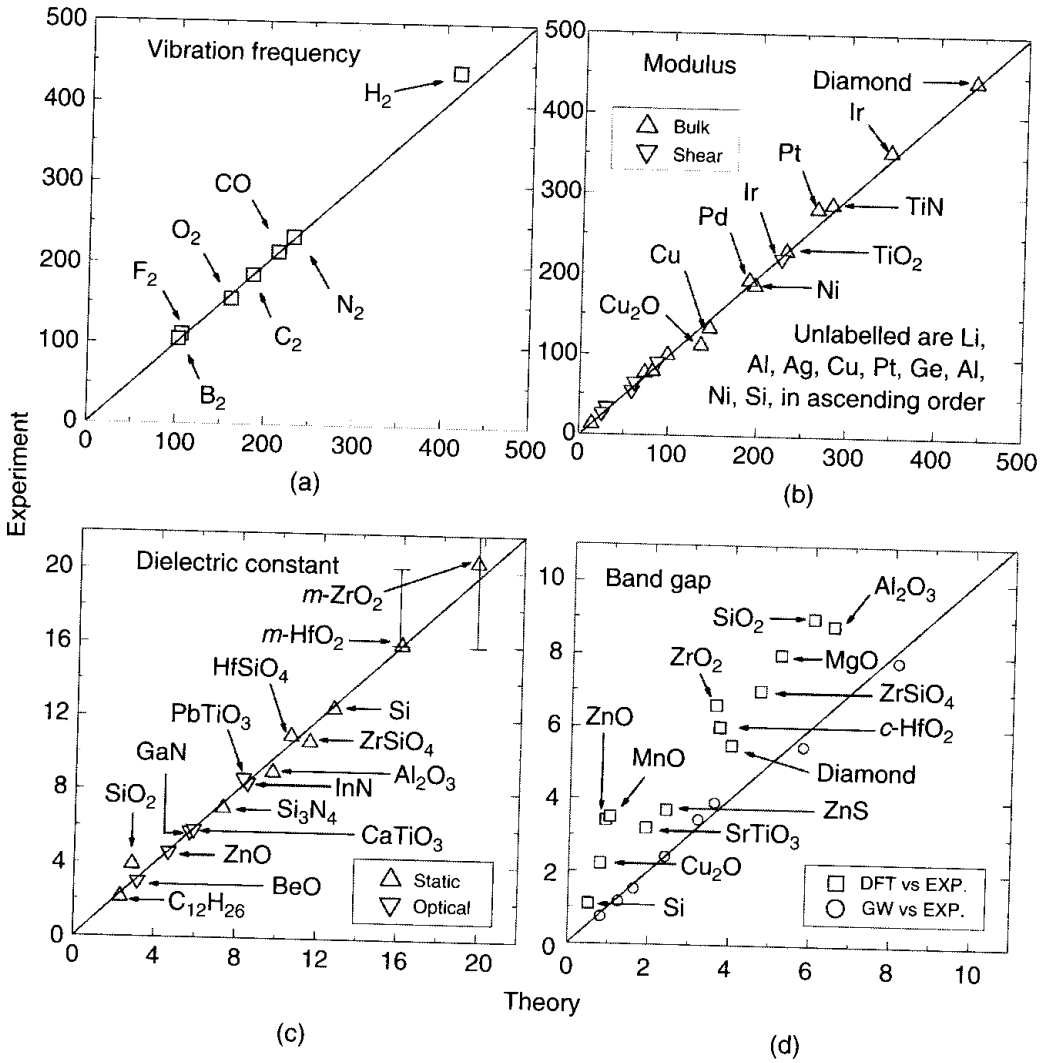

Figure 11.2 Comparison between DFT predictions (horizontal axes) and experimental values (vertical axes) [30]. (Reprinted with permission from R. Ramprasad, N. Shi, and C. Tang. Modeling the physics and chemistry of interfaces in nanodielectrics. In Dielectric Polymer Nanocomposites. J. K. Nelson (Ed.), Springer (2010). Copyright 2010 by Springer). Comparisons for (a) vibrational frequencies of diatomic molecules, (b) bulk and shear moduli of solids, (c) static and optical dielectric constants of insulators, and (d) band gaps of insulators. Frequencies are in cm^{-1}, elastic moduli in gigapascals, and band gaps in electron volts. Data are from various sources including References 28, 29, 31–33. Data for *GW* method in (d) are from Reference 34.

One should always bear in mind that the real surfaces of solids, even when they have no foreign contaminants, are seldom perfect two-dimensional planes. Rather, they contain many imperfections (such as surface vacancies and adatoms), steps, facets, islands, etc., as illustrated schematically in Figure 11.3. To a first approximation, one can assume that when a perfect crystal is sliced along a plane, none of the remaining atoms moves from its original location in the crystal and a perfect crystalline behavior is maintained from the surface throughout the bulk.

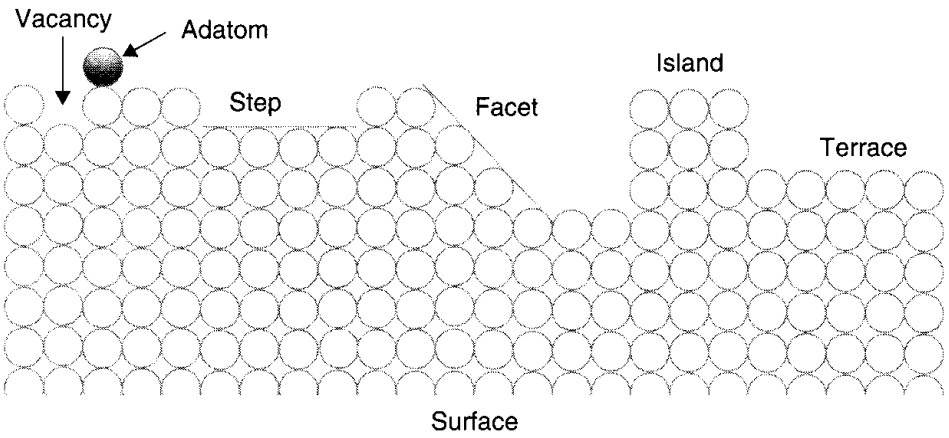

Figure 11.3 A schematic illustration depicting a microscopic view of a surface. In "real-life" situations, a surface of any material may significantly deviate from its idealistic bulk-terminated geometry and often contains zero-, one-, and two-dimensional defects; surface adsorbates; etc. (*See insert for color representation of the figure.*)

However, this idealized bulk-terminated surface assumption is never true in practice. In fact, there is no reason that the material near the surface should retain the same bulk-like interlayer distance, given that the coordination of atoms near the surface is significantly reduced compared to that in the bulk. It is generally observed that the interlayer spacing near the surface is always somewhat different from that in the bulk. This phenomenon is known as *surface relaxation*, which results in only a mild deformation of the crystal at the surface with a slight increase or decrease of the volume per atom near the surface. Relaxation effects generally affect several atomic layers at the surface. A surface layer exposing at least two types of atoms on the surface may also rumple, owing to the different strengths of the surface relaxation for the different atoms. Forces acting at the surface that give rise to surface relaxations and changes in the bonding and interlayer spacing of the surface atoms to different degrees may result in more dramatic effects such as the rearrangement of atoms along the surface or interface plane. Such changes are referred to as *surface reconstruction*. Surfaces of metallic solids generally exhibit a much weaker tendency to reconstruct as reduced coordination on the surface can easily be made up through redistribution of the delocalized electron gas. However, this phenomenon is much more pronounced in the case of covalently bonded semiconductor surfaces (e.g., Si, Ge, CdSe, GaAs, etc.) in which loss of nearest neighbors is rather difficult to compensate for except through passivation of dangling bonds by rehybridization of surface atoms followed by rearrangement of these atoms on the surface.

11.4 THE SURFACE ENERGY AND ISSUES WITH POLAR SURFACES

Any theoretical prediction of stable surface orientation, termination, and reconstruction is made through computation of the Gibb's surface free energy (γ),

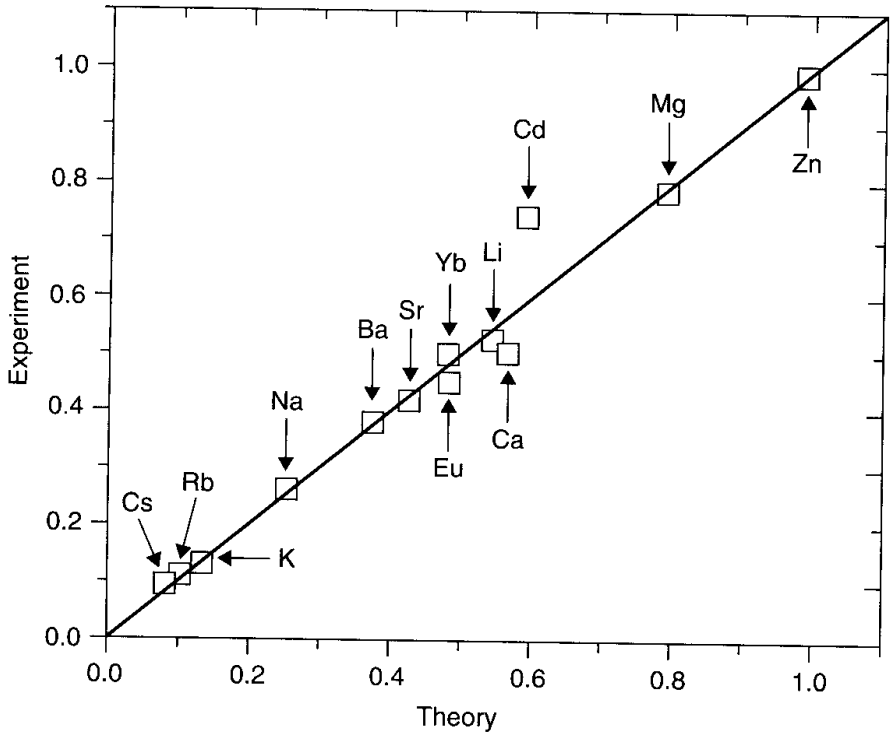

Figure 11.4 Comparison of DFT-computed surface energy (in J/m^{-2}) with experiments for the most stable surface orientations for various materials [38]. (Data collected from L. Vitos, A.V. Ruban, H.L. Skriver, and J. Kollar, Surf. Sci, 1998, 411, 186.)

which can be calculated by subtracting the total Gibbs free energy of a slab from that of the appropriate bulk reference. However, for a solid state system at low temperatures and pressures, one can, to a good approximation, replace the Gibbs free energy with the internal energy of the system, neglecting contributions from configurational and vibrational entropies. The internal energy can be directly computed from the first principles electronic structure calculations. For an elemental system, or for a slab of a compound system containing an integer number of formula units, the surface energy can be defined as

$$\gamma = \frac{1}{A}(E_{\text{slab}} - NE_{\text{bulk}}), \tag{11.2}$$

Here, A is the total area for the top and bottom surfaces of the slab, E_{slab} is the total energy of the supercell containing the surface model in the slab geometry, and N stoichiometric units of the bulk (with energy E_{bulk}) have been used to construct the supercell. This strategy has been used to reliably compute the surface energy for a variety of elemental slab surfaces, as shown in Figure 11.4. [38]

However, one should note that it is not always possible to construct a stoichiometric as well as a symmetric slab with identical terminations at the top and bottom of the slab. Usually, in compound materials (containing more than one constituting element), a stoichiometric slab model may contain nonidentical

top and bottom surfaces. For example, in a stoichiometric slab model of a (001) surface in a cubic ABO_3 type perovskite structure, the top and bottom surfaces will have AO- and BO_2-terminations. In such situations, the above expression for the surface energy provides the average surface energy of the top and bottom surfaces.

Another peculiar problem that arises in the case of an asymmetric periodically repeated slab is the appearance of an unphysical electric field in the vacuum region between the slab and its periodic image. To eliminate this artificial electric field in the vacuum region, one may introduce a dipole layer in the midvacuum region that exactly cancels out the electric field created by the normal component of the dipole moment of the slab. Alternatively, one may switch to a symmetric slab geometry with identical top and bottom surfaces. However, in that case, the slab will be nonstoichiometric and will require the introduction of a chemical potential to uniquely define the surface energy of the specific terminating surface. For such a nonstoichiometric slab system composed of n constituents within a supercell containing N_i atoms and with a μ_i chemical potential of the i_{th} constituent, the surface energy γ can be written as follows:

$$\gamma = \frac{1}{A}(E_{\text{slab}} - \sum_{i}^{n} N_i \mu_i) \tag{11.3}$$

Although the determination of the exact value of μ of each species may be difficult, following simple thermodynamic stability arguments, one can easily derive the allowed range for μ for each of the constituent. Also note that the chemical potential μ of each component depends both on temperature and pressure. We first deal with zero temperature and pressure conditions. The generalizations to the finite temperature and pressure situations is discussed in Section 11.7.

The basic aspects of surface relaxations and issues surrounding surface energy determinations can be understood using a II-VI semiconductor such as CdSe. The surface facets of wurtzite CdSe can mainly be classified as either polar or nonpolar, depending on the stoichiometry of the atoms contained in the surface plane. The nonpolar surfaces are stoichiometric, containing equal numbers of Cd and Se atoms in each surface plane, and carry a net zero dipole moment along the surface normal. The three most stable nonpolar surface facets of CdSe, viz., $(10\bar{1}0)$, $(01\bar{1}0)$, and $(11\bar{2}0)$, are considered for the present illustration. Polar facets, on the other hand, are composed of nonstoichiometric planes of either only Cd or only Se atoms and therefore carry a nonzero component of the surface dipole moment along the slab normal. For a further detailed classification of polar versus nonpolar facets, the readers are referred to a recent review by Goniakowski et al. [39].

The unrelaxed bulk-terminated and the DFT-optimized surface geometries for the polar and nonpolar CdSe facets are shown in Figure 11.5. The relaxation behavior of these facets can, in general, be understood through the electron counting rules for II-VI semiconductor systems [40]. Since Cd and Se have nominal valences of 2 and 6, respectively, sp^3 hybridization in bulk CdSe requires that

a Cd atom contributes 1/2 electron to each of its four bonds to Se and an Se atom contributes 3/2 electrons to each of its four bonds to Cd. Atoms at a surface display lower coordination, and hence unshared electrons. By suitable relaxation and reconstruction, a surface attempts to minimize its energy by optimally sharing the electrons at the surface, that is, by rehybridizing, and the extent to which this is accomplished will depend on the nature of the surface and the number of unshared electrons. In the case of the nonpolar $(01\bar{1}0)$, $(10\bar{1}0)$, and $(11\bar{2}0)$ surfaces, significant relaxation is observed. In general, comparison of initial and relaxed structures shows that surface Cd atoms move inward toward the bulk and the surface Se atoms tend to move outward, resulting in a tilting of the surface CdSe bond relative to the horizontal. This tilting of the CdSe bond on relaxation can be understood in terms of the transfer of electrons from the Cd atoms to the more electronegative Se atoms at the surface. We note that, in the case of the $(01\bar{1}0)$ surface, each surface atom displays two dangling bonds, while the $(10\bar{1}0)$ and $(11\bar{2}0)$ surface atoms display one dangling bond each. Thus, Cd atoms at $(10\bar{1}0)$ and $(11\bar{2}0)$ surfaces can donate their unshared 1/2 electron to the surface Se atoms, resulting in a more planar threefold sp^2-type configuration around the surface Cd atom accompanied by the inward movement of surface Cd atoms. The surface Se atoms, on the other hand, possess a doubly filled dangling bond, which is preferentially exposed to any incoming electronegative species. A similar, but more intensified, process occurs at the $(01\bar{1}0)$ surface, as the surface atoms contain two dangling bonds to begin with. Thus, the $(01\bar{1}0)$ surface relaxation is more pronounced. In the case of the polar (0001)Cd, $(000\bar{1})$Cd, (0001)Se, and $(000\bar{1})$Se surfaces—the first two being terminated purely by Cd atoms and the other two by purely Se atoms—no significant relaxation was observed. As these surfaces have only one type of atomic species (either Cd or Se, with one or three dangling bonds), transfer of electrons from the dangling bonds is not possible, and hence there is no clear pathway available for relaxation. Thus, the extent of surface relaxation for polar facets is found to be significantly smaller than those of nonpolar facets.

For a CdSe crystal in thermodynamic equilibrium, the sum of the chemical potential of Cd (μ_{Cd}) and Se (μ_{Se}) atoms should be equal to the chemical potential of the bulk CdSe (μ_{CdSe}). Furthermore, the respective chemical potentials of the constituents (i.e., Cd or Se) at the surface and in the bulk of the crystal have to be the same to avoid any macroscopic mass exchange between the bulk and the surface. Thus, it follows that

$$\begin{aligned} \mu_{Cd}^{bulk} &= \mu_{Cd}^{surface} = \mu_{Cd} \\ \mu_{Se}^{bulk} &= \mu_{Se}^{surface} = \mu_{Se}. \end{aligned} \tag{11.4}$$

One can further make the important observation that the chemical potential of the Cd and Se atoms in CdSe should always be less than the chemical potential of the condensed phases in their respective elemental form (represented as $\mu_{Cd}^{Cd,bulk}$ and $\mu_{Se}^{Se,bulk}$ for Cd and Se, respectively), else the CdSe crystal will become

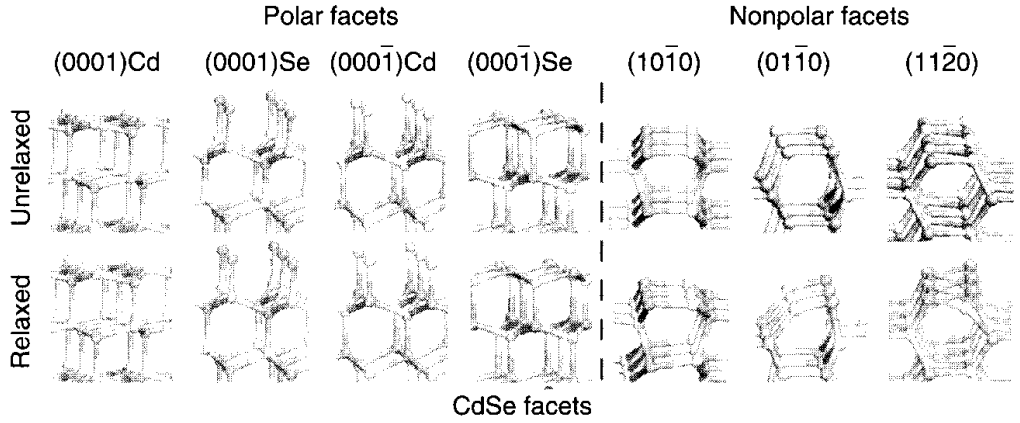

Figure 11.5 Atomistic models of the polar (0001)Cd, (0001)Se, (000$\bar{1}$)Cd, and (000$\bar{1}$)Se and nonpolar (10$\bar{1}$0), (01$\bar{1}$0), and (11$\bar{2}$0) facets of wurtzite CdSe in the bulk-terminated unrelaxed (top) and the relaxed states (bottom).

thermodynamically unstable against its decomposition into respective bulk phases of its atomic reservoirs, that is,

$$\begin{aligned} \mu_{\mathrm{Cd}} &< \mu_{\mathrm{Cd}}^{\mathrm{Cd,bulk}} \\ \mu_{\mathrm{Se}} &< \mu_{\mathrm{Se}}^{\mathrm{Se,bulk}} \end{aligned} \tag{11.5}$$

However, one should also note that the $\mu_{\mathrm{Cd}}^{\mathrm{Cd,bulk}}$ and $\mu_{\mathrm{Se}}^{\mathrm{Se,bulk}}$ are related to the μ_{CdSe} through the heat of formation of CdSe crystal (ΔH_{CdSe}) via

$$\mu_{\mathrm{CdSe}} = \mu_{\mathrm{Cd}}^{\mathrm{Cd,bulk}} + \mu_{\mathrm{Se}}^{\mathrm{Se,bulk}} + \Delta H_{\mathrm{CdSe}} \tag{11.6}$$

Combining Equations (11.5) and (11.6), one can obtain the allowed range of chemical potentials of μ_{Cd} and μ_{Se} in the CdSe crystal as

$$\begin{aligned} \mu_{\mathrm{Cd}}^{\mathrm{Cd,bulk}} + \Delta H_{\mathrm{CdSe}} < \mu_{\mathrm{Cd}} < \mu_{\mathrm{Cd}}^{\mathrm{Cd,bulk}} \\ \mu_{\mathrm{Se}}^{\mathrm{Se,bulk}} + \Delta H_{\mathrm{CdSe}} < \mu_{\mathrm{Se}} < \mu_{\mathrm{Se}}^{\mathrm{Se,bulk}} \end{aligned} \tag{11.7}$$

We define the two extreme values for μ_{Cd} as those related to a Cd atom in a "Cd-poor" CdSe crystal (corresponding to minimum μ_{Cd} or maximum μ_{Se}) and in a "Cd-rich" CdSe crystal (corresponding to maximum μ_{Cd} or minimum μ_{Se}). We further make a note that although the allowed range of μ_{Cd} can be properly defined, identification of the value corresponding to specific chemical conditions is nontrivial. For instance, based on the Gibbs–Thompson equation one can easily see that the chemical potential will vary with the size of a nanocrystal [41].

The surface energy of the nonpolar facets can be easily calculated using Equation 11.2. However, determination of the chemical-potential-dependent surface energies of the four polar facets of the wurtzite CdSe is not straightforward

because of the absence of inversion symmetry. Note that of the four inequivalent {0001} polar surface facets of wurtzite CdSe, two (i.e., (0001)Cd and (0001)Se) can occur exclusively on one side terminated purely by Cd or by Se atoms and the other two (i.e., $(000\bar{1})$Cd and $(000\bar{1})$Se) on the opposite side in a slab geometry, again terminated purely by Cd or Se atoms. Furthermore, owing to the inherent asymmetry between the positive and negative c-axes, the (0001)Cd and the (0001)Se facets have one and three dangling bonds, respectively. On the other hand, the $(000\bar{1})$Cd and the $(000\bar{1})$Se facets have three and one dangling bonds, respectively. Therefore, it is possible to construct four different types of slab geometries, and, in principle, one can calculate the four unknown surface energies of the polar facets. However, it turns out that such a construction will lead to only three linearly independent equations, which can be further manipulated to give rise to the fourth one. Therefore, owing to the lack of inversion symmetry in the wurtzite crystal structure, the (0001) and $(000\bar{1})$ surface energies cannot be isolated independently using a slab geometry. A similar problem arises for the polar (111) and $(11\bar{1})$ surfaces of the zinc blende structure. For this crystal structure, however, a method of direct calculation of the surface energies has been developed by Zhang and Wei [42] that requires construction of one-dimensional wedge-shaped structures for extracting surface energies. This method has also been applied to CdSe [43, 44] to estimate the surface energy of the polar facets in the wurtzite phase under the plausible assumption that the (0001) and $(000\bar{1})$ facets of the hexagonal wurtzite structure are atomically identical to the (111) and $(11\bar{1})$ facets of the zinc blende structure. Following the technical details described in Reference 44, surface energies of all the four polar facets can be calculated.

The DFT-calculated surface energies of all the relaxed surface facets are plotted in Figure 11.6 over the allowed range of μ_{Cd} values. As already mentioned, the surface energies of nonpolar surfaces do not depend on μ_{Cd} (shown by the dashed lines) and therefore show up as horizontal lines in the plot. Interestingly, the two nonpolar surfaces with one dangling bond per surface atom, $(10\bar{1}0)$ and $(11\bar{2}0)$, have the lowest surface energy, while the surface energy of the $(01\bar{1}0)$ facet, with two dangling bonds per surface atom, is almost double that of the latter ones. The surface energy of the polar facets with one and three dangling bonds is shown as solid and dotted-dashed lines, respectively, in the plot and is a linear function of μ_{Cd}. However, note that the average of surface energies for the two pairs of polar facets, is always constant. Furthermore, the stability of the Cd-terminated polar surfaces increases as we move from Cd-poor to Cd-rich conditions, while the Se-terminated polar surfaces display the opposite behavior. Comparison of the polar surfaces with three dangling bonds per surface atom reveals that the $(000\bar{1})$Cd surface is more stable than the (0001)Se surface throughout the range of chemical potential considered. On the other hand, in the case of polar surfaces with one dangling bond per surface atom, the $(000\bar{1})$Se surface is more stable.

We close this section by indicating that reliable DFT-based schemes are available for computing the surface energies of elemental as well as multicomponent

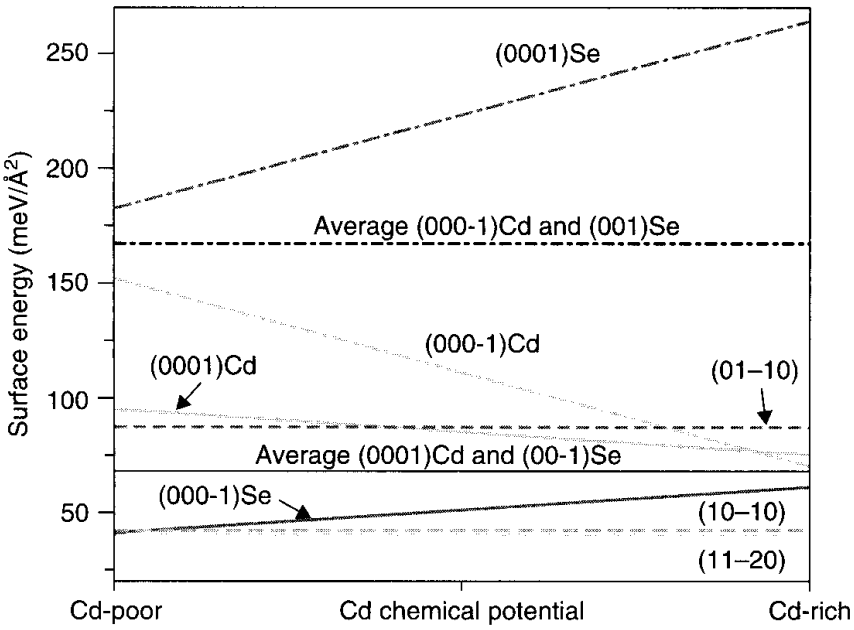

Figure 11.6 Surface energies for polar and nonpolar wurtzite CdSe facets as a function of Cd chemical potential (μ_{Cd}^{CdSe}). (*See insert for color representation of the figure.*)

systems. The shape of a crystal is in fact controlled by the anisotropic nature of the surface energies (i.e., because of different surfaces displaying different surface energies). The concept of manipulating the shape of crystallites and controlling the growth of nanostructures through modulating the surface energies, for example, through adsorbates, is discussed in the next section.

11.5 ADSORBATE ON SURFACES—ENERGETICS AND THE WULFF CONSTRUCTION

Surface adsorption is a phenomenon of key importance in surface science and dominates many chemical processes. To obtain a microscopic understanding of the role of adsorbates, it is necessary to know the surface atomic structure. Most of the early structural studies of surface adsorption assumed implicitly that the surface provided a rigid platform of identical adsorption sites, which did not change during the course of adsorption, onto which atoms or molecules were adsorbed. However, it is now well understood that a surface can modify the behavior of adsorbed species in many direct and indirect ways, for instance, through bond breakage, charge transfer, long-range ordering effects and adsorbate–adsorbate lateral interactions. It has also become clear, of course, that the adsorbate also induces changes in the substrate surface. Surface reconstruction, extent of surface relaxation, and surface rumpling are usually strong functions of the type and coverage of surface adatoms or molecules.

Adsorbates also affect the morphology of crystallites through alteration of the surface energies. To understand this, one should note that the equilibrium

shape of a crystal is determined by the anisotropic surface energies via the Wulff construction [45, 46]. Determination of the equilibrium shape of crystals that minimizes the total surface free energy proceeds by the following three steps: (i) determination of the surface energies for various facets experimentally or theoretically; (ii) drawing vectors normal to the crystal facets from a common origin, with the length proportional to the surface energies; and (iii) creating at the end of each vector a plane perpendicular to the vector. The shape enclosed by the planes gives the equilibrium shape of the crystal. First principles calculations are playing an increasingly important role in this field, partly due to the capability of such methods to accurately determine surface energies and partly due to the difficulty in quantitatively determining the surface or interface energy experimentally. Some interesting insights have been achieved in the past. For example, using DFT calculations, Shi and Stampfl [47] illustrated that the equilibrium shape of a Au catalyst particle changes with the O_2 atmosphere, with the predominant terminations changing from (111) to (110) with increasing O_2 pressure or decreasing temperature.

In the following sections, we illustrate how the crystal shape and morphology may be controlled through surface energy and surface adsorption using three specific examples: (i) oxygen adsorption on wurtzite CdSe facets, (ii) hydroxyl adsorption on the low-index facets of rocksalt MgO, and (iii) metal adsorption on hexagonal tungsten carbide (WC) surfaces.

11.5.1 CdSe Crystallites

Quantification of the bonding strength of an adsorbate on a substrate is generally done in terms of binding energy (E_b) as

$$E_b = (E_{surf,Ad} - E_{surf,clean} - n_{Ad}\mu_{Ad,gas})/n_{Ad}, \tag{11.8}$$

where n_{Ad} is the number of adsorbate species (atoms or molecules) adsorbed per surface unit cell and $\mu_{Ad,gas}$ is the chemical potential of adsorbate in the reference gas phase (usually taken as the DFT total energy of the gaseous adsorbate molecule). $E_{surf,Ad}$ and $E_{surf,clean}$ are the total energies of the surface models with and without surface adatoms on the surface of interest, respectively.

Knowing the surface energy of the clean surface facet (γ_{clean}) from Equation 11.2 or 11.3, the surface energy of the adatom covered-surface (γ_{Ad}) is obtained by

$$\gamma_{Ad} = \gamma_{clean} + n_{Ad}E_b/A, \tag{11.9}$$

where A is the area of the surface unit cell. It is clear from the above equation that the surface energy for adsorbate-passivated surface facets (which eventually determines equilibrium shape and morphology of the growing crystals) is a function of binding energy, which in turn depends on the temperature, pressure,

chemical environment, and surface coverage of adatoms. Therefore, by controlling the growth environment and selecting appropriate surface adsorbates, one can control the equilibrium shape of the crystal. This can be particularly important for oxygen-containing (or water-vapor-containing) environments, where the stability of different surface facets of varying stoichiometry may well be anticipated as a function of oxygen (or hydroxyl groups) in the surrounding gas phase. The surface energy of CdSe facets was discussed in the previous section. CdSe is one of the most technologically important II-VI semiconductors. One-dimensional (1D) nanocrystals of CdSe (i.e., CdSe quantum rods) possess unique optical properties such as linearly polarized emission and higher Stokes shift when compared to zero-dimensional nanocrystals such as quantum dots [48, 49]. From a device standpoint, it is more desirable to have a larger aspect ratio of quantum rods along with the ability to engineer heterojunctions, which renders 1D nanostructures of CdSe more advantageous than the quantum dots [50–54].

An interesting and potentially useful phenomenon observed in wurtzite CdSe nanocrystals is asymmetric anisotropic growth in the presence of oxygen (captured schematically in Figure 11.7a). While anisotropic growth in wurtzite systems refers to preferred growth along one dimension (say, the c-axis) over others, asymmetric anisotropic growth refers to a strong preference to grow along only one of the two complementary anisotropic axes (say, along the positive c-axis rather than along the negative c-axis). As already mentioned, these systems display four inequivalent {0001} surface facets, exclusively occurring in pairs on the either side. Note that for any preferential one-dimensional growth, both the surface facets, that occur in a complementary pair on that side, should have high surface energy. Therefore, growth along one direction will be controlled by one pair of surfaces, while growth along the opposite direction will be controlled by a different pair of surfaces.

Although experimental studies [56] had suggested that oxygen might have a role in directing the growth of CdSe nanocrystals to quantum rods, the underlying mechanism and various factors controlling the asymmetric growth of wurtzite nanostructures were discussed in detail by Pilania et al. [44], based on the results of their ab initio computations. DFT-based surface energy calculations of various polar and nonpolar facets of CdSe showed that both ordering and relative magnitude of these facets change on oxygen adsorption. It was quite crucial to note that the unidirectional and unidimensional growth along the [0001] direction can occur only through successive and interconvertible creation of (0001)Cd and (0001)Se surfaces. Thus, for vigorous growth to occur preferentially along the (0001) direction, the surface energy of both the (0001)Cd and (0001)Se surfaces should necessarily be high relative to that of all other surface facets. Even if one of these two surfaces has a low surface energy, growth along the (0001) direction will be hindered. In fact, the calculated results revealed that both the (0001)Cd and (0001)Se surfaces display large positive values of the surface energy relative to all other surfaces for a large range of allowed Cd chemical potential values (μ_{Cd}, which was used to quantify environmental growth conditions), indicating the possibility of preferential growth along the (0001) direction

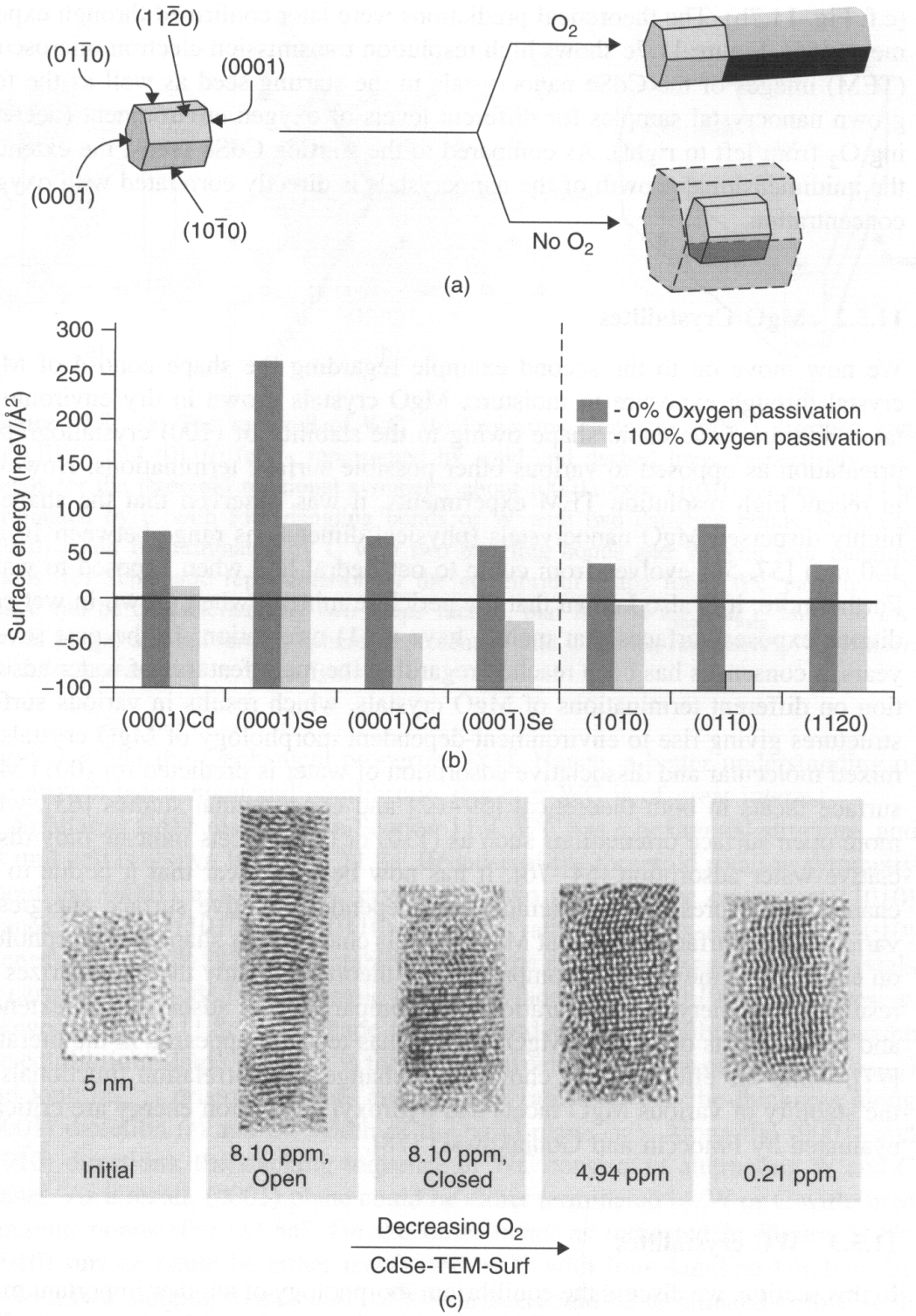

Figure 11.7 (a) Schematic illustration depicting the role of oxygen environment on the growth of wurtzite CdSe nanocrystals. (b) DFT-calculated surface energies for the polar and nonpolar wurtzite CdSe facets before and after oxygen passivation. (c) High resolution transmission electron microscopy images of representative CdSe nanocrystals for various oxygen concentrations. The 5 nm scale bar shown in the leftmost panel applies to all images [55]. (*See insert for color representation of the figure.*) (Reprinted with permission from J. D. Doll, G. Pilania, R. Ramprasad, and F. Papadimitrakopoulos, Nano Lett., 2010, 10, 680. Copyright 2010 American Chemical Society.)

(c.f. Fig. 11.7b). The theoretical predictions were later confirmed through experiments [55]. Figure 11.7c shows high resolution transmission electron microscopy (TEM) images of the CdSe nanocrystals in the starting seed as well as the four grown nanocrystal samples for different levels of oxygen environment (decreasing O_2 from left to right). As compared to the starting CdSe seeds, the extent of the unidimensional growth of the nanocrystals is directly correlated with oxygen concentration.

11.5.2 MgO Crystallites

We now move on to the second example regarding the shape control of MgO crystal through exposure to moisture. MgO crystals grown in dry environmental conditions have cubic shape owing to the stability of (100) crystallographic orientation as opposed to various other possible surface terminations. However, in recent high resolution TEM experiments, it was observed that the shape of highly dispersed MgO nanocrystals (physical dimensions range between 10 and 100 nm) [57, 58] evolves from cubic to octahedral-like when exposed to water. Furthermore, it is also known that the periclase mineral when grown in wet conditions exposes surfaces that mainly have (111) orientation. In the past several years, a consensus has been reached regarding the main features of water adsorption on different terminations of MgO crystals, which results in various surface structures giving rise to environment-dependent morphology of MgO crystals. A mixed molecular and dissociative adsorption of water is predicted for (001) MgO surface facets in both theoretical [59–62] and experimental studies [63], while more open surface orientations such as (110) or (111) facets indicate only dissociative water adsorption [64–76]. It has now become clear that it is due to the change in the pressure- and temperature-dependent relative surface energies of various MgO surface facets that MgO crystals change their shape and morphology on exposure to moisture. A comprehensive theoretical study that summarizes the results for a variety of configurations and compares water adsorption on extended and point defects on various MgO surfaces has recently appeared in the literature [77], while the effects of the choice of exchange and correlation functionals on the stability of various MgO facets and hydroxyl adsorption energy are critically evaluated by Finocchi and Goniakowski [78].

11.5.3 WC crystallites

In this section, we discuss the equilibrium morphology of another important material, WC, under different conditions (i.e., various surface adsorbates as well as carbon concentrations), determined based on DFT results and the Wulff theorem [79]. As important hard metal components, WC-based cermets (WC crystals embedded in a secondary binder phase, such as Co) have been widely used in military and in aerospace, automotive, and marine industries [80]. However, there is strong evidence showing that the size and shape of WC crystals within the

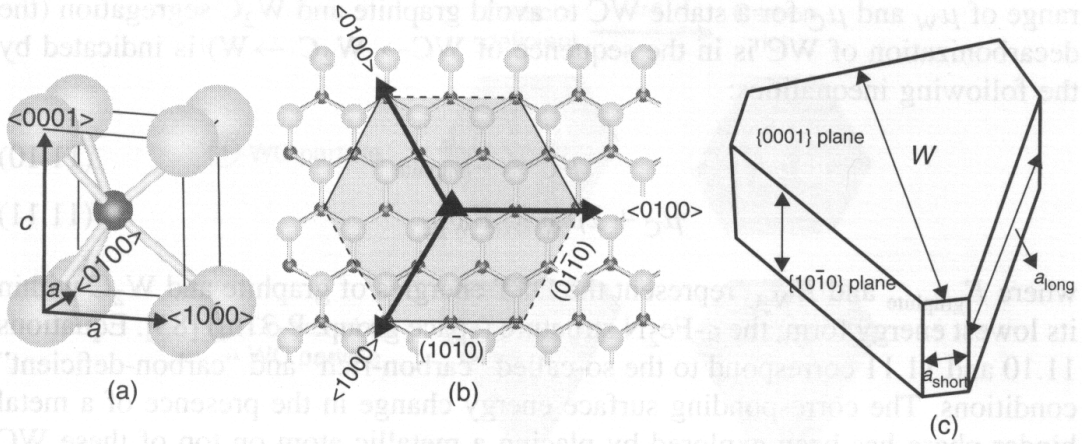

Figure 11.8 (a) The unit cell of WC. (b) Projection along the ⟨0001⟩ direction with the (10$\bar{1}$0) and (01$\bar{1}$0) facets represented by solid and dashed lines, respectively. "△" stands for the threefold rotational symmetry about ⟨0001⟩ axis. (10$\bar{1}$0) surface could be terminated by C with four dangling bonds or W with two dangling bonds. Similarly, (10$\bar{1}$0) could be terminated by C with two dangling bonds and W with four dangling bonds. (c) Schematic representation of the equilibrium shape for a WC particle. The shape can be characterized by two shape factors, that is, $r = a_{short}/a_{long}$ and $k = t/w$. Green (large) and red (small) spheres represent W and C atoms, respectively. (*See insert for color representation of the figure*.)

cermets affect the mechanical properties [81]. Hence, a better understanding of the growth mechanism and equilibrium shape of WC is of great interest.

Similar to CdSe discussed in Section 11.4, WC has a hexagonal structure, and its unit cell is shown in Figure 11.8a. Because of the threefold rotation symmetry about the ⟨0001⟩ axis, the WC crystal has two sets of three equivalent {10$\bar{1}$0} planes, namely, (10$\bar{1}$0) and (01$\bar{1}$0) surfaces, rather than six equivalent {10$\bar{1}$0} planes (Fig. 11.8b) [82]. It is established that the shape of hexagonal WC crystals in cermets is bounded by prismatic {10$\bar{1}$0} surfaces and basal {0001} surfaces, as shown in Figure 11.8c. Two shape factors r and k are normally used to describe the equilibrium shape, where r is the ratio between the lengths of the short (a_{short}) and long (a_{long}) prismatic facets and k is the ratio between the thickness along ⟨0001⟩ direction (t) and the width of the basal plane (w). Along the ⟨0001⟩ and ⟨10$\bar{1}$0⟩ directions, the stacking sequence of WC consists of alternating W and C planes. As a result, (0001) plane could be either terminated by W or C with three dangling bonds (Fig. 11.8a). On the other hand, as indicated in Figure 11.8b, (10$\bar{1}$0) surface could be either terminated by C with four dangling bonds or by W with two dangling bonds and (01$\bar{1}$0) surface could be terminated with C with two dangling bonds or W with four dangling bonds. We should note that although each W (or C) is bonded to six neighboring C (or W) atoms, when projected onto (0001) plane, half the bonds are on top of the others and thus not shown in Figure 11.8b.

The energies of these clean surfaces could be computed based on Equation 11.3 with $\mu_i = \mu_W$ and μ_C by adopting nonstoichiometric supercells. The allowed

range of μ_W and μ_C for a stable WC to avoid graphite and W_2C segregation (the decarbonization of WC is in the sequence of WC$\rightarrow$ W_2C $\rightarrow$W) is indicated by the following inequalities:

$$\mu_C < E_{\text{graphite}} \tag{11.10}$$

$$\mu_C + 2\mu_W < E_{W_2C} \tag{11.11}$$

where E_{graphite} and E_{W_2C} represent the DFT energies of graphite and W_2C within its lowest energy form, the ϵ-Fe_2N structure (space group: P-31m) [83]. Equations 11.10 and 11.11 correspond to the so-called "carbon-rich" and "carbon-deficient" conditions. The corresponding surface energy change in the presence of a metal binder phase has been explored by placing a metallic atom on top of these WC surfaces. Co and Ni, as the most common binder materials for WC, have been already explored as discussed below.

The lowest energies of each of the (0001)-, $(10\bar{1}0)$- and $(01\bar{1}0)$-type surfaces along with Wulff theorem determined the equilibrium crystal shape at different conditions in Figure 11.9. Several interesting points are found from this figure. (i) As expected, the crystal shape and its factors vary with the surface conditions (i.e., clean WC surface, Co-adsorbed WC surface, and Ni-adsorbed surface). (ii) At the same surface condition, the chemical potential of carbon affects the equilibrium shape of WC particles. (iii) Co adsorption under the carbon-deficient condition promotes the formation of truncated triangular prisms, whereas Ni adsorption under the carbon-rich condition enhances the formation of near-hexagonal prisms. (iv) The equilibrium shapes of WC crystals under all conditions (especially with Co or Ni adsorption) can be described as "bulky" because their k factors are close to 0.8 or are higher, and thus the thickness of the truncated triangular prism and the width of its basal plane are similar, which is far from the platelet geometry.

Figures 11.10a,b show the SEM images for WC–Co powders in the carbon-rich and carbon-deficient conditions, respectively. Although the shape of large particles may or may not be the equilibrium morphology of WC particles, depending on whether the crystal growth is controlled kinetically or thermodynamically, it is still beneficial to compare the shape of the large particles in the experiments with the simulation results. Note that the truncated triangular prism has appeared in both types of powders. However, r factors for the two powders are different. For the carbon-rich powder (Fig. 11.10a), the short prismatic facets are approximately ~0.4 times the length of the long prismatic facets, which is close to the theoretical prediction shown in Fig. 11.9. For the carbon-deficient powder (Fig. 11.10b), the r factor from the SEM image is in the range of 0.2 ~ 0.3, which is also in good agreement with the theoretical value, 0.23 (Fig. 11.9). These results reveal that the chemical potential of carbon can affect the morphology of WC particles. However, the ratios of the thickness of the truncated WC prism to the width of the basal plane, that is, the k factor, in both powders are smaller than those predicted from the first principles calculation (Fig. 11.9), which may be caused by the slow growth kinetics along the [0001] direction.

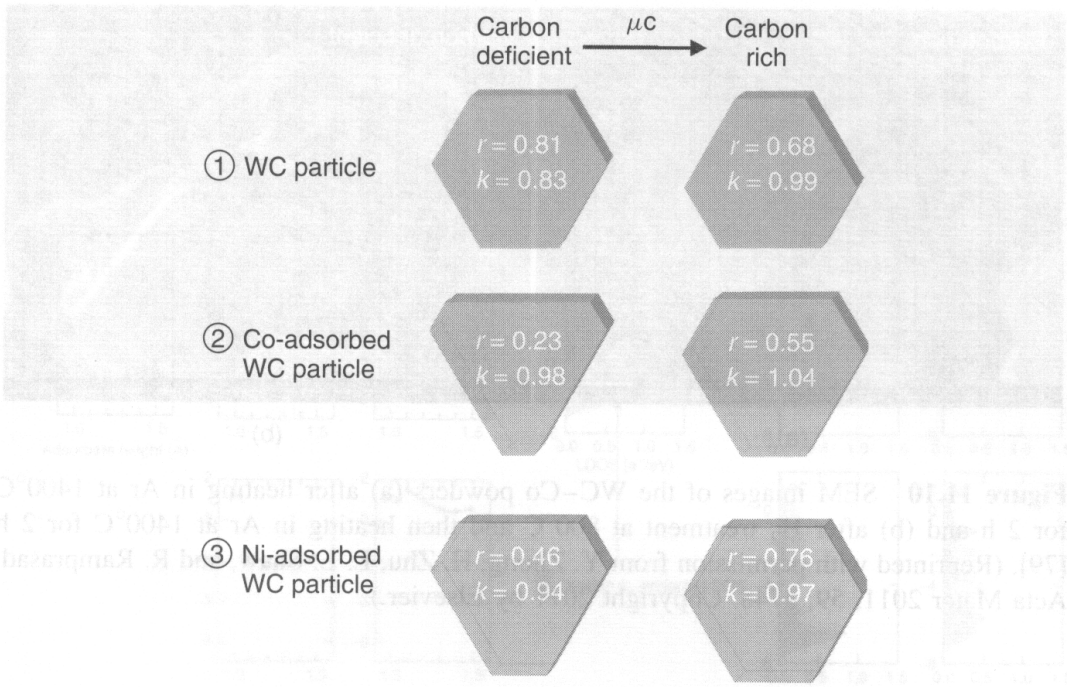

Figure 11.9 The equilibrium shapes for pure WC, Co-adsorbed WC, and Ni-adsorbed WC particles in carbon-rich and carbon-deficient conditions. The two factors, k and r, are also indicated.

In light of the difficulties in experimentally identifying the correlation between morphologies and factors such as surface adsorbates, temperature, pressure, and bulk compositions, etc. DFT-based Wulff construction is becoming a useful tool in this arena.

11.6 ADSORBATES ON SURFACES—ELECTRONIC STRUCTURE

In the previous section, we discussed applications of DFT-based techniques to study the structure and energetics of surfaces at the atomistic level. Now, we discuss the local electronic structure of atomic and molecular adsorbates on the surface. The properties and reactivity of an adsorbed atom or molecule are determined by the nature of the surface chemical bond, which in turn is governed by the newly formed electronic states because of the bonding to the surface. Interaction of an incoming adsorbate with the surface can vary from being very weak (i.e., physisorption) to strong enough such that it actually rearranges the valence levels of the adsorbate (i.e., chemisorption). Discrete and sharp molecular/atomic orbitals in case of an isolated gaseous adsorbate gradually evolve on its interaction with the substrate (and also with other neighboring adsorbates) to produce a new set of electronic states/bands that are usually broadened and energetically shifted with respect to the gas-phase species. In the following discussion, we shed some light on how informative and potentially important local

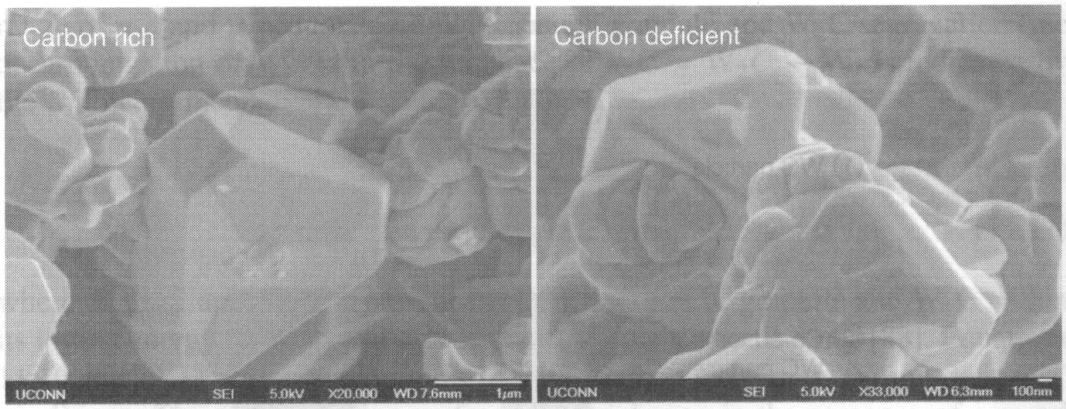

Figure 11.10 SEM images of the WC–Co powders (a) after heating in Ar at 1400°C for 2 h and (b) after H_2 treatment at 800°C and then heating in Ar at 1400°C for 2 h [79]. (Reprinted with permission from Y. Zhong, H. Zhu, L. L. Shaw, and R. Ramprasad, Acta Mater 2011, 59, 3748. Copyright 2011 by Elsevier.)

density of states (LDOS) could be in the case of surface adsorption to probe local electronic structure. For the sake of illustration, we take a specific example of atomic oxygen adsorption on various transition metal surfaces with the aim of understanding trends in oxygen adsorption energies on the metal surfaces.

Figure 11.11a shows DFT-calculated adsorption energies as a function of the distance of the O atom above the surface for various transition metals in a small section of the periodic table. The more negative the binding energy, the stronger is the bond between oxygen adsorbate and the metal surface. The energy per oxygen atom in a gaseous O_2 molecule is shown for comparison. Only metals in which the minimum in the adsorption energy function is below this value will be able to dissociate O_2 exothermally. It can be seen that O binds most strongly to the metals to the left in the transition metal series and more strongly to the 3d metals than to the 4d and 5d metals. It is evident from Figure 11.11a that with O adatoms, Ru bonds much stronger than Pd and Ag. Au is very noble with a bond energy per O atom less than that of O_2, Ag is just able to dissociate O_2 exothermically, and Cu forms quite strong bonds. It is also noted that these DFT-calculated results are in excellent agreement with the experimental findings [1].

However, before we try to understand this trend in the oxygen adsorption energy for various transition metal surfaces through LDOS and local electronic structure, it is important to note that the valence states of the transition metal surface atoms can be divided up into the free-electron-like s electron states and the more localized d electron states. Following the Newns–Anderson model [85, 86], the interaction of the adsorbate atom with the delocalized s electrons leads to a broad resonance, whereas interaction with the narrow band d states leads to distinct new bonding and antibonding levels (cf. Fig. 11.12).

To simplify, one can imagine this complex coupling between the adsorbate atomic level to the metal s and d states to be composed of various discrete steps.

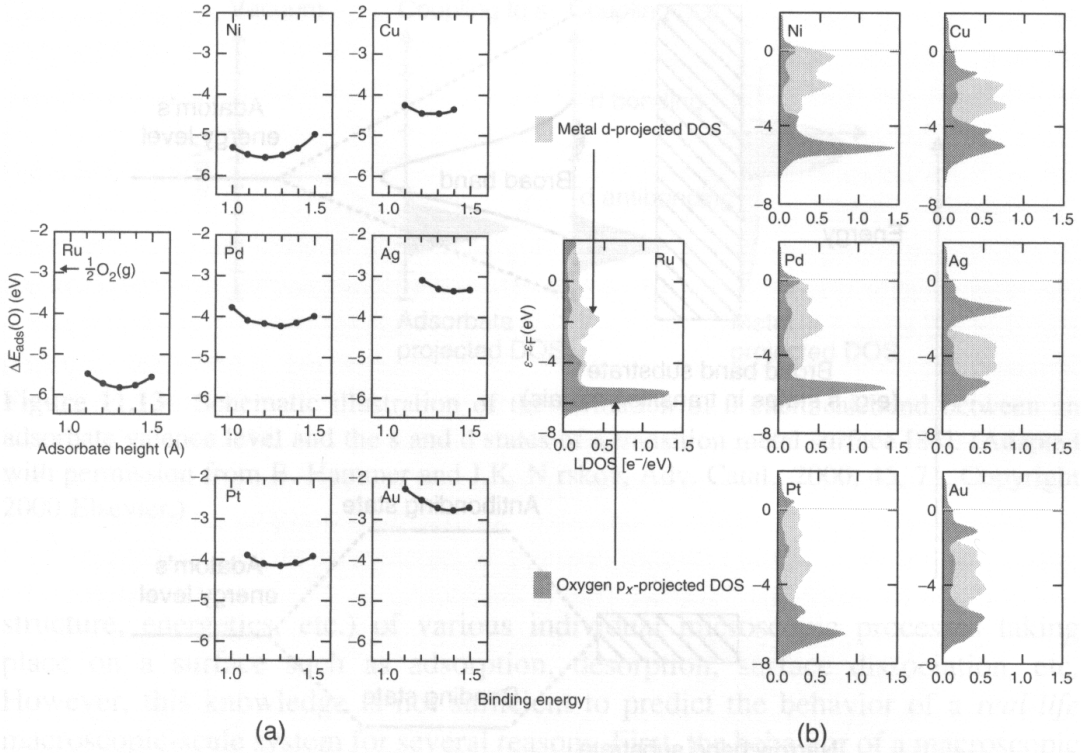

Figure 11.11 (a) DFT-calculated adsorption energy for oxygen adatom as a function of distance of the O adatom above the surface for a range of close-packed transition metal surfaces, ordered according to their position in the periodic table. The energy per O atom in gaseous O_2 is also shown in the leftmost box, showing results for Ru for comparison. (b) The density of states projected onto the d states (gray) of the surface atoms for the surfaces considered in (a). The oxygen $2p^x$ projected density of states (black) for adsorbed O adatom on the same surfaces are also shown. The formation of bonding and antibonding states below and above the metal d states is clearly seen [84]. (Adapted with permission from B. Hammer and J.K. N rskov, Adv. Catal., 2000, 45, 71. Copyright 2000 Elsevier.)

First, let us consider coupling of the adsorbate atomic levels with the metal's s states, and in the next step, we switch on the coupling to the metal d states as well. The coupling to the broad s band in the first step leads to a broadening and shift of the adsorbate state (Fig. 11.13). Usually there are only small differences in this interaction going from one transition metal to the other, owing to the fact that all the transition metals have a half-filled considerably broad s band in the metallic state. Therefore, the differences between the different transition metals must be associated primarily with the d states. The interaction of the adsorbate states with localized d states will give rise to the formation of separate bonding and antibonding states, as shown in the bottom of Figure 11.13. In such a picture, bonding strength of an adsorbates depends on the relative occupancy of bonding and antibonding states. The strength of the bond will be maximum when the bonding states are completely occupied and all the antibonding states are empty, whereas if the antibonding states also start getting filled, the bond gradually becomes weaker.

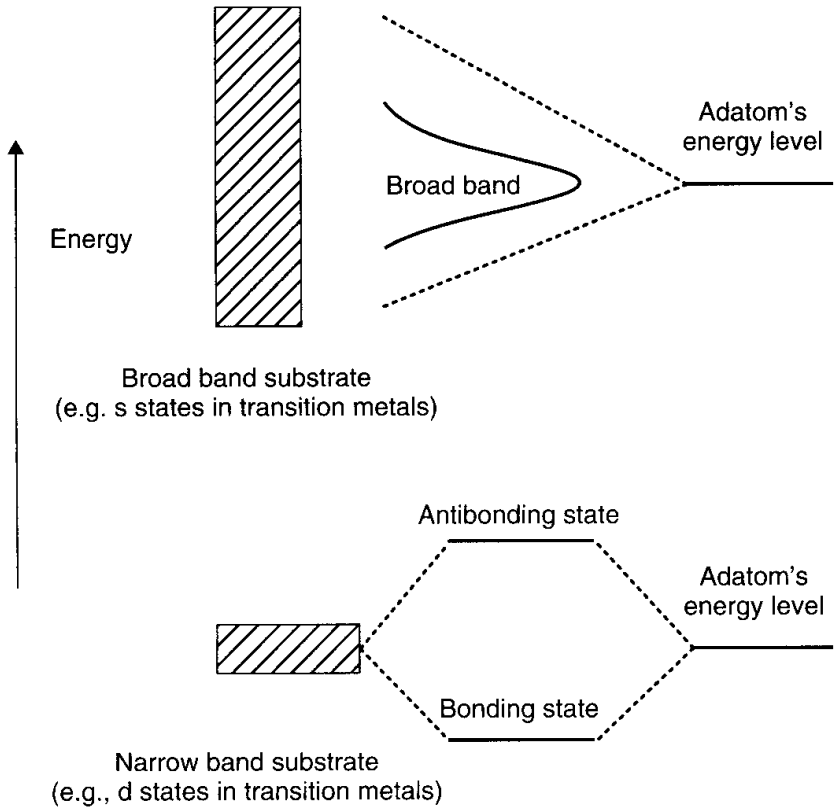

Figure 11.12 Schematic diagram depicting evolution of the projected density of states of an adsorbate as it gets adsorbed onto a surface within the Newns–Anderson model [85, 86] in two limiting cases: when the band width is large (top) and when the band width is small (bottom).

To understand the variations in the binding energy of oxygen adatom, let us look at the variations in the electronic structure of the oxygen adsorbed on the different transition metals (Fig. 11.11b). Since the energy of the d states relative to the Fermi level varies substantially from one metal to the next, the number of antibonding states that are above the Fermi level, and thus empty, will depend on the transition metal under consideration. It can be seen that the antibonding states for oxygen adatom get filled gradually as we move from Ru to Pd to Ag, explaining why the bonding becomes weaker in that order. However, the above picture is not sufficient to understand why 3d metals bond stronger than 4d and 5d metals. More extensive models have been developed to explain these effects and to extend this theory for more complex systems [84, 87].

11.7 SURFACE PHASE DIAGRAMS: FIRST PRINCIPLES THERMODYNAMICS

From the above discussion, it is clear that first principles computational techniques can provide an adequate description (in terms of geometrical and electronic

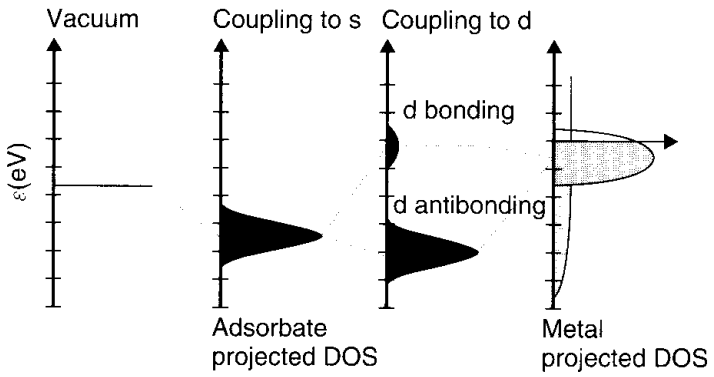

Figure 11.13 Schematic illustration of the formation of a chemical bond between an adsorbate valence level and the s and d states of a transition metal surface [84]. (Adapted with permission from B. Hammer and J.K. N rskov, Adv. Catal., 2000, 45, 71. Copyright 2000 Elsevier.)

structure, energetics, etc.) of various individual microscopic processes taking place on a surface such as adsorption, desorption, surface dissociation, etc. However, this knowledge is not sufficient to predict the behavior of a *real-life* macroscopic-scale system for several reasons. First, the behavior of a macroscopic system of any technological relevance is usually governed by a large number of distinct atomic scale processes. Therefore, in addition to the precise description of elementary processes involved, any predictive modeling of a macroscopic system would also require information regarding statistical interplay of a large number of such possible microscopic processes. In other words, we are interested not only in each individual elementary process taking place in isolation but also in what happens when a large number of such processes are allowed to take place simultaneously. Second, in the microscopic regime, electronic excitations and lattice vibrations in a material take place on time scales of femtoseconds and picoseconds, respectively, while bond breaking and bond formation occur at a length scale of several angstroms. On the other hand, in the macroscopic regime, relevant times are of the order of 10^{-3} to several hundreds of seconds and the relevant length scales can vary from 10^{-6} to several meters. To obtain macroscopically observable system properties and functions from electronic structure theories such as DFT, a gap of several orders of magnitude in *both* time and length scales will have to be overcome. Finally, in the electronic structure calculations, the pressure and temperature effects are not included. Therefore, to actually describe the situations of finite temperatures and pressures, first principles calculations have to be used as an input for further thermodynamic considerations. In the following paragraphs, we discuss how such a description, appropriate for the macroscopic regime, can be achieved by combining the results of ab initio DFT with concepts from statistical mechanics and thermodynamics.

The primary aim of the first principles atomistic thermodynamics approach is to use information pertaining to the potential energy surface calculated at the level of electronic structure theory, for a system in equilibrium (or in a meta

stable state), to calculate an appropriate thermodynamic potential function such as the Gibbs free energy G. The Gibbs free energy of any system decomposed in terms of various contributing factors can be given as follows:

$$G(T, P) = E^{\mathrm{DFT}} + F^{v} - TS^{\mathrm{c}} + PV. \tag{11.12}$$

In this equation, the leading term E^{DFT} represents the internal energy of the system and can be obtained directly from electronic structure theory calculations. The second term represents the vibrational free energy, which contains contributions due to *both* the zero point energy E^{ZPE} and the vibrational entropy. The third term is the configurational free energy arising from the configurational entropy S^{c}. T, P, and V are the temperature, pressure, and volume, respectively. Once this pressure- and temperature-dependent Gibbs free energy is known, one is immediately in a position to calculate all the macroscopic properties of the system of interest. Although this concept is quite general and applicable to a broad range of problems, here we find it instructive to illustrate the approach by taking a specific example of a metal surface in equilibrium with the surrounding oxygen environment.

As already mentioned, in an ab initio atomistic thermodynamic approach, we are interested only in the equilibrium state (or metastable state) of the system and not in the information as to how the system has evolved to reach that state. Therefore, the first task of the present thermodynamic approach would naturally be to identify a number of known (based on the experimental information available in the literature) and unknown but possibly relevant (based on the computational screening) oxygen-containing surface structures along with the clean and bulk oxide surface structures. Once the time-consuming electronic structure calculations are done, the next step is to evaluate which of the considered surface structures are most stable and at what environmental conditions (i.e., the temperature and partial pressure of O_2). Therefore, much of the remaining discussion in the present section is based on a nonzero T and P generalization of Equation 11.3.

For a two-components system composed of metal M and oxygen, the (T,P)-dependent surface free energy γ is a function of the chemical potential of the metal (μ_{M}) and oxygen (μ_{O})

$$\gamma(T, P) = \frac{1}{A}[G^{\mathrm{surf}}(T, P, N_{\mathrm{M}}, N_{\mathrm{O}}) - N_{\mathrm{M}}\mu_{\mathrm{M}}(T, P) - N_{\mathrm{O}}\mu_{\mathrm{O}}(T, P)], \tag{11.13}$$

where N_{M} and N_{O} are the number of metal and oxygen atoms in the finite supercell of the system that repeats to a produce 2D infinite slab. The chemical potentials of the metal at the surface and in the bulk of the crystal have to be same to avoid any macroscopic mass exchange between the bulk and the surface, and therefore, for a sufficiently thick metallic slab, it is fixed to the corresponding bulk value, $\mu_{\mathrm{M}} = \mu_{\mathrm{M}}^{\mathrm{bulk}}$. Oxygen chemical potential on the other hand is a variable that can cover a range of values and plays a decisive role in

stabilizing a particular surface structure. Under ultrahigh vacuum, when oxygen chemical potential μ_O is very low, the clean metal surface prevails, and this situation is known as O-poor limit. On the other hand, O-rich limit is defined by $\mu_O = 1/2E_{O_2}^{DFT}$, with $E_{O_2}^{DFT}$ being the DFT-calculated total energy of an O_2 molecule in the gas phase. If μ_O exceeds this critical limit, condensation of the O_2 molecule from the gas phase to the surface will take place. Furthermore, when considering a metal surface in contact with O_2, a complete conversion of the metal into a bulk oxide phase is also a thermodynamic possibility that should be taken into account. Therefore, the stability of the corresponding bulk oxide (let us say M_xO_y) has to be evaluated with respect to the various other surface oxide adlayer-containing structures. In the bulk oxide phase, the chemical potential of the metal and oxygen do not remain independent any more and are related to the Gibbs free energy of the bulk oxide ($g_{M_xO_y}^{bulk}$) as

$$x\mu_M(T, P) + y\mu_O(T, P) = g_{M_xO_y}^{bulk}(T, P). \tag{11.14}$$

Furthermore, thermodynamic stability of the oxide phase requires that $\mu_M(T, p) \leq g_M^{bulk}(T, P)$; otherwise, the surface oxide will decompose back into the solid metal and the oxygen gas phases. Using this constraint along with Equation 11.14 and taking $T = 0$ K and $P = 0$ atm limit for the bulk phase energies, we can find the minimum oxygen chemical potential $\min[\mu_O(T, P)]$ at which formation of the bulk oxide phase will indeed become thermodynamically favorable, as

$$\min[\mu_O(T, P)] = \frac{1}{y}[g_{M_xO_y}^{bulk}(0, 0) - xg_M^{bulk}(0, 0)]. \tag{11.15}$$

So far, we have seen how the surface free energy and therefore, the thermodynamic stability of various surface structures varies as a function of oxygen chemical potential for a metallic surface in equilibrium with oxygen reservoir. Furthermore, we have also established the bounds on the valid range of the oxygen chemical potential based on thermodynamic stability arguments. However, a quantitative evaluation of surface free energy requires evaluation of each and every component of the Gibbs free energy, as described in Equation 11.12. As already mentioned, the leading term in the Gibbs free energy expression is the total energy E^{tot}, which has to be evaluated directly from the electronic structure theory calculations. The remaining terms in the expression (viz., the vibrational term, the configurational entropy, and the PV-term) are discussed below.

Calculation of the configurational entropy is quite involved and very much system specific. To explicitly treat the configuration contribution to the total free energy, one has to sample the configurational space of all ordered and disordered structures using modern statistical methods such as Monte Carlo simulations. However, when dealing with highly crystalline structures such as metals or metal oxides with moderately disordered surfaces, the configurational entropic contributions are usually quite small and can be estimated as follows.

Let us assume that the system under consideration has N surface sites with n identical defects or adsorbate sites. Then the total number of ways in which the surface can be configured is given by $\omega = \frac{(N+n)!}{N!n!}$. From statistical mechanics, the configurational entropy of such a system is given by

$$S^{c} = k_{B} \ln \omega = k_{B} \ln \frac{(N+n)!}{N!n!}, \tag{11.16}$$

where k_B is the Boltzmann constant. Now, in addition to using the Sterling approximation ($ln(n!) = nln(n) - n, n \gg 1$), we estimate the total surface area A by summing up the areas of all surface sites (NA_{site}), assuming only a small concentration of defects. Then the configurational entropic contribution per unit area is given by

$$\frac{TS^{c}}{A} = \frac{k_{B}T}{A_{site}} \left[ln\left(1 + \frac{n}{N}\right) + \frac{n}{N} ln\left(1 + \frac{N}{n}\right) \right]. \tag{11.17}$$

Assuming that for a moderately disordered surface the ratio of (n/N) remains with in 5%, Equation 11.17 gives

$$\frac{TS^{c}}{A} \leq 0.20 \frac{k_{B}T}{A_{site}}. \tag{11.18}$$

For temperatures as high as 1000 K and surface areas per site of about 16 Å^2, the configurational entropy will not contribute more than about 1 meV/Å^2 to the surface free energy, and therefore, to a first approximation, this contribution is often neglected. However, it is important to note that for highly disordered systems as well as for various phase boundaries, this contribution to the Gibbs free energy of the surface will not be negligible, and in such cases, the exact contribution has to be calculated using Monte Carlo simulations.

The vibrational contribution is typically computed at the harmonic level (with the quasiharmonic and anharmonic contributions generally ignored). Even the harmonic contribution is rather expensive to compute for large systems. What is determined is the phonon density of states (DOS) $\sigma(\omega)$ for the bulk and relevant surface structures. Once the harmonic phonon DOS is known, the vibrational contribution to the Gibbs free energy can be written as

$$F^{v} = \int \sigma(\omega) \left[\frac{1}{2} \hbar\omega + k_{B}T \ \ln(1 - e^{-\hbar\omega/k_{B}T}) \right] d\omega. \tag{11.19}$$

However, it is often useful to first obtain an estimation of magnitude of the vibrational contribution to the surface Gibbs free energy before calculating the cumbersome full phonon DOS. In the calculation of the surface free energy, the term F^{v} contains the change in the vibrational modes of the surface atoms or surface adsorbates with respect to their bulk counterparts. As the vibrational modes of atoms in the interior of the surface are not expected to change much because of

the formation of surface or surface adsorption or defect formation, the term F^{v} can usually be safely estimated by considering only the change in the vibrational modes of atoms in the topmost layer of the slab and the surface adsorbates with respect to the bulk within the Einstein model of harmonic approximation.

The contribution to the Gibbs free energy due to the last term (i.e., the PV term) in Equation 11.12 is in general negligible for solids. It is easy to see through a simple dimensional analysis that the term PV/A (atm Å^3/Å^2) $\sim 10^{-3}$ meV/Å^2. Even at very high pressures such as 100 atm, the PV term contributes only 0.1 meV/Å^2, which can be safely neglected in comparison with the total surface free energy term, which is usually of the order of 100 meV/Å^2.

An example plot of the surface energy γ as a function of the chemical potential of the surrounding gas phase conveniently defined in terms of $\Delta\mu_O = \mu_O(T, P) - 1/2E_{O_2}^{DFT}$ is shown in Figure 11.14a, while Figure 11.14b shows the schematics of various stable thermodynamic phases for a metal surface in equilibrium with O_2 reservoir, as the oxygen chemical potential varies from a very low to a very high value within allowed bounds. The surface free energy of a clean metal surface will be independent of the gas-phase chemical potential and shows up as a horizontal line on the plot. As one can easily guess, at the lower end of the oxygen chemical potential, the clean metal surface will be the most favored thermodynamic phase, and therefore have the lowest surface free energy. As the oxygen chemical potential gradually increases, more and more oxygen would get adsorbed on the surface. As the oxygen content of the surface increases, the slope of the γ v/s $\Delta\mu_O$ curve gets more and more negative, leading to the formation of stable surface phases I and II and eventually, at the critical oxygen chemical potential (cf. Eq. 11.15), formation of the bulk oxide phase takes place. Increasing the oxygen chemical potential even further would finally lead to oxygen condensation onto the oxidized metal surface (at $\mu_O = 1/2E_{O_2}^{tot}$). We also note that the width of the thermodynamic stability range of the bulk oxide phase on the oxygen chemical potential axis is given by the heat of formation of the bulk oxide (min[$\mu_O(T, P)$]-1/2 $E_{O_2}^{tot} = \frac{1}{y}\Delta G^{f}_{M_xO_y}(0, 0)$); in other words, the width is equal to the stability of the bulk oxide per oxygen atom.

11.8 INTERFACE PHASE DIAGRAMS: FIRST PRINCIPLES THERMODYNAMICS

The determination of the surface phase diagrams when systems are in equilibrium with appropriate gas phase molecules using FPT constitutes a reasonably mature computational methodology in materials research as discussed in the previous sections. In following paragraphs, we discuss the usefulness of this methodology to predict the interface phase diagram using Si-HfO_2 and Pt-HfO_2 interfaces as examples. These two types of interfaces—-found in the sub-45 nm complementary metal oxide semiconductor (CMOS) technology, based on high dielectric constant (or "high-k") oxides and metal electrodes—present a set of issues related to the interface oxidation, morphology, and defect chemistry [88, 89].

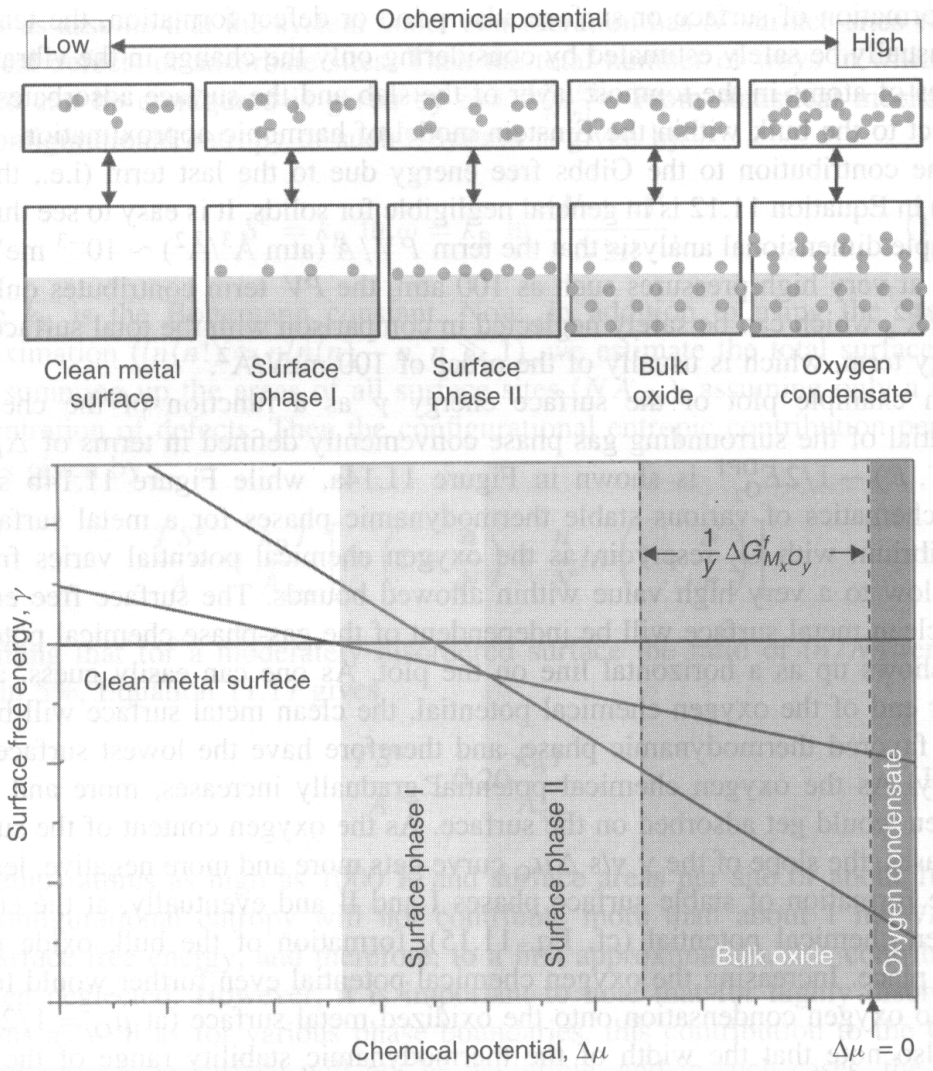

Figure 11.14 Example plot of Gibbs surface free energy (γ) versus oxygen chemical potential ($\Delta\mu_O = \mu_O(T, P) - 1/2E^{\mathrm{DFT}}_{O_2}$) for a surface in equilibrium with a surrounding gas phase. The surface energy of the clean metal surface serves as a zero reference in the plot. Adsorption of an O adatom will become favorable on the metal surface only if the Gibbs free energy of the resultant oxygen adatom-covered surface is lower than that of the clean surface. Also note that as the O content of the surface increases, the slope of the γ versus $\Delta\mu_O$ plot becomes increasingly negative. With increasing gas-phase chemical potential, first the clean metal phase is stable, then the first and second adsorbate phases become stable followed by an oxide phase, and finally, oxygen gas phase condensation takes place on the surface. (*See insert for color representation of the figure.*)

In the case of the Si-HfO_2 interface, a low-k SiO_x or metallic silicide phase (both of which are undesirable) could form at Si-HfO_2 interfaces [88, 90, 91]. In fact, reversible formation of SiO_x and silicides at the Si-HfO_2 interface by annealing in oxygen-rich and oxygen-deficient environments, respectively, have been observed previously [92, 93]. On the other hand, the desired metal electrodes should possess appropriate work functions such that the metal Fermi level

lines up with either the valence or conduction band edges of the underlying Si substrate. However, the interfacial chemistries at metal-HfO_2 interfaces (in terms of charge transfer, bond formation, defect accumulation, dipole creation, etc.) lead to shifts in the work function value from its true vacuum value [94] and shows a dependence on the processing conditions. Thus, in both cases of Si-HfO_2 and metal-HfO_2 interfaces, it would be valuable to understand the relationship between ambient conditions (e.g., temperature and oxygen pressure) and interface morphologies.

Figure 11.15 shows the standard interface supercells containing an X-HfO_2 (X = Si or Pt) heterostructure and a vacuum region. The interface oxidation could be modeled by varying the concentration of O at the X-HfO_2 interface, which is represented by θ_O in units of a monolayer (ML). In keeping with the stoichiometry of HfO_2, an ML is defined as two times the number of Hf atoms in a layer (1 ML of O has 4 O atoms in the specific interface

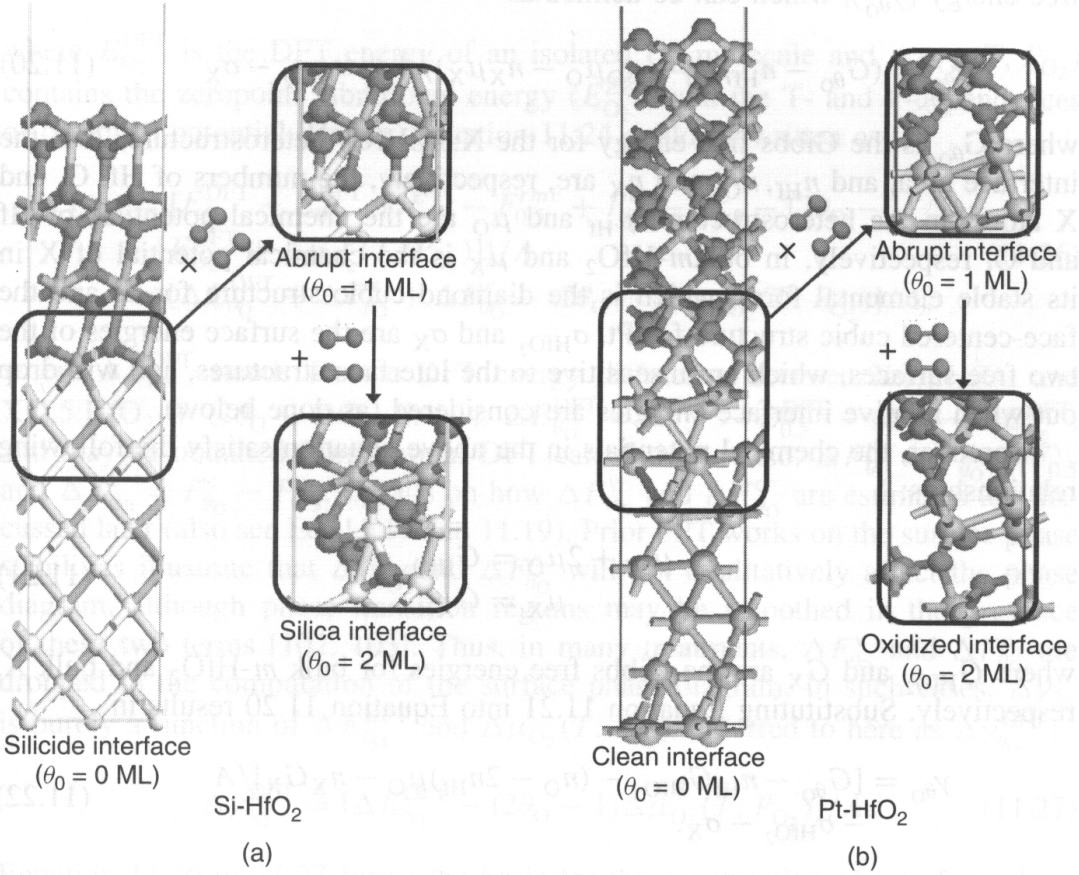

Figure 11.15 The representative atomic structures of the X-HfO_2 heterostructures with X at the bottom: (a) Si-HfO_2 interface and (b) Pt-HfO_2 interface. The Hf and O atoms of the top HfO_2 parts in both (a) and (b) are represented by light blue (gray) and red (dark) spheres, respectively [99]. (*See insert for color representation of the figure.*) (Reprinted with permission from H. Zhu, C. Tang, and R. Ramprasad, Phys Rev, 2010, B 82, 235413 and H. Zhu and R. Ramprasad, Phys. Rev,2011, B 83, 081416(R). Copyright 2010 by the American Physical Society.)

models considered). The corresponding interface configurations are denoted by X:θ_O:HfO_2. Three representative interfaces for Si-HfO_2 and Pt-HfO_2 are indicated in Figure 11.15a,b. For Si-HfO_2, $\theta_O = 0$ corresponds to an interface completely depleted of O and is thus composed of primarily Hf-Si bonds; we refer to this as a "silicide" interface. A well-passivated Si-HfO_2 interface requires a full ML of O, with half of the ML passivating HfO_2 and the other half passivating Si [95]. This situation is referred as an *abrupt interface* ($\theta_O = 1$). $\theta_O > 1$ represents a situation in which O atoms in excess of 1 ML prefer to penetrate the Si side of the heterostructure, with the most favorable sites being between the top two Si layers [96–98]; we refer to this as an *oxidized interface*. When $\theta_O = 2$, the interface is a silica-like interface. Similarly, the three representative interfaces for Pt-HfO_2, Pt:0:HfO_2, Pt:1:HfO_2, and Pt:2:HfO_2 are referred to as *clean, abrupt, and oxidized interfaces*, respectively (see 11.15b).

We now describe the approach used to create the interface phase diagrams based on FPT [99]. The most stable interface is the one with minimum interface free energy (γ_{θ_O}), which can be defined as

$$\gamma_{\theta_O} = (G_{\theta_O} - n_{Hf}\mu_{Hf} - n_O\mu_O - n_X\mu_X)/A - \sigma_{HfO_2} - \sigma_X \tag{11.20}$$

where G_{θ_O} is the Gibbs free energy for the X:θ_O:HfO_2 heterostructure, A is the interface area, and n_{Hf}, n_O, and n_X are, respectively, the numbers of Hf, O, and X atoms in the heterostructure. μ_{Hf} and μ_O are the chemical potentials of Hf and O, respectively, in bulk$m$-HfO_2 and μ_X is the chemical potential of X in its stable elemental form, which is the diamond cubic structure for Si and the face-centered cubic structure for Pt. σ_{HfO_2} and σ_X are the surface energies of the two free surfaces, which are insensitive to the interface structures, and will drop out when relative interface energies are considered (as done below).

Moreover, the chemical potentials in the above equation satisfy the following relationships:

$$\begin{aligned} \mu_{Hf} + 2\mu_O &= G_{HfO_2} \\ \mu_X &= G_X, \end{aligned} \tag{11.21}$$

where G_{HfO_2} and G_X are the Gibbs free energies for bulk m-HfO_2 and bulk X, respectively. Substituting Equation 11.21 into Equation 11.20 results in

$$\begin{aligned} \gamma_{\theta_O} = [G_{\theta_O} - n_{Hf}G_{HfO_2} - (n_O - 2n_{Hf})\mu_O - n_X G_X]/A \\ - \sigma_{HfO_2} - \sigma_X. \end{aligned} \tag{11.22}$$

When $\theta_O = 0.5$, the whole system is stoichiometric ($n_{Hf} : n_O = 1{:}2$) and the interface energy is

$$\gamma_{0.5} = (G_{0.5} - n_{Hf}G_{HfO_2} - n_X G_X)/A - \sigma_{HfO_2} - \sigma_X. \tag{11.23}$$

By using $\gamma_{0.5}$ as a reference, replacing $n_O - 2n_{Hf}$ by $4 \times (\theta_O - 0.5)$ (four accounts for the fact that 1 ML of O contains four atoms in the interfaces

considered here, see Fig. 11.15), substituting Equation 11.12 into Equations 11.22 and 11.23, and assuming that the PV terms for X:θ_O:HfO_2 and X:0.5:HfO_2 are roughly equivalent, the relative interface energy can be further defined as

$$\begin{aligned}\Delta\gamma_{\theta_O} &= \gamma_{\theta_O} - \gamma_{0.5} \\ &= [E^{DFT}_{\theta_O} - E^{DFT}_{0.5} + F^{v}_{\theta_O} - F^{v}_{0.5} + F^{c}_{\theta_O} - F^{c}_{0.5} \\ &\quad - 4(\theta_O - 0.5)\mu_O]/A.\end{aligned} \tag{11.24}$$

The X:θ_O:HfO_2 heterostructure reaches its equilibrium state at a certain temperature and oxygen pressure by exchanging O atoms with the surrounding atmosphere. Hence, μ_O in Equation 11.24 could be replaced with half of the chemical potential of an oxygen molecule, μ_{O_2}, which is a function of temperature (T) and oxygen pressure (P_{O_2}), and could be obtained from JANAF tables or ab initio statistical mechanics [100, 101].

$$\mu_{O_2}(T, P_{O_2}) = E^{DFT}_{O_2} + \Delta\mu_{O_2}(T, P_{O_2}), \tag{11.25}$$

where $E^{DFT}_{O_2}$ is the DFT energy of an isolated O_2 molecule and $\Delta\mu_{O_2}(T, P_{O_2})$ contains the zeropoint vibrational energy ($E^{ZPE}_{O_2}$) and the T- and P-dependences of chemical potential. Hence, Equation 11.24 could be written as

$$\begin{aligned}\Delta\gamma_{\theta_O} &= \{E^{DFT}_{\theta_O} - E^{DFT}_{0.5} + F^{v}_{\theta_O} - F^{rmv}_{0.5} + F^{c}_{\theta_O} - F^{c}_{0.5} - (2\theta_O - 1) \\ &\quad [E^{DFT}_{O_2} + \Delta\mu_{O_2}(T, P_{O_2})]\}/A \\ &= [\Delta E^{DFT}_{\theta_O} + \Delta F^{v}_{\theta_O} + \Delta F^{c}_{\theta_O} - (2\theta_O - 1)\Delta\mu_{O_2}(T, P_{O_2})]/A,\end{aligned} \tag{11.26}$$

where $\Delta E^{DFT}_{\theta_O}$ stands for the DFT energy difference between X:θ_O:HfO_2 and X:0.5:HfO_2 + $(2\theta_O - 1)O_2$, that is, $\Delta E^{DFT}_{\theta_O} = E^{DFT}_{\theta_O} - E^{DFT}_{0.5} - (2\theta_O - 1)E^{DFT}_{O_2}$, and may be obtained from normal DFT calculations. Also, $\Delta F^{v}_{\theta_O} = F^{v}_{\theta_O} - F^{v}_{0.5}$ and $\Delta F^{c}_{\theta_O} = F^{c}_{\theta_O} - F^{c}_{0.5}$. Details on how $\Delta F^{v}_{\theta_O}$ and $\Delta F^{c}_{\theta_O}$ are estimated are discussed later (also see Eq. 11.17 and 11.19). Prior FPT works on the surface phase stabilities illustrate that $\Delta F^{v}_{\theta_O}$ and $\Delta F^{c}_{\theta_O}$ will not qualitatively affect the phase diagram, although phase transition regions may be smoothed in the presence of these two terms [102, 103]. Thus, in many treatments, $\Delta F^{v}_{\theta_O}$ and $\Delta F^{c}_{\theta_O}$ are dropped in the computation of the surface phase diagram. In such cases, $\Delta\gamma_{\theta_O}$ is purely a function of $\Delta E^{DFT}_{\theta_O}$ and $\Delta\mu_{O_2}(T, P_{O_2})$ (referred to here as $\Delta\gamma^{DFT}_{\theta_O}$).

$$\Delta\gamma^{DFT}_{\theta_O} = [\Delta E^{DFT}_{\theta_O} - (2\theta_O - 1)\Delta\mu_{O_2}(T, P_{O_2})]/A. \tag{11.27}$$

Equation 11.26 or 11.27 forms the basis for the construction of interface phase diagrams, from which one can compute the interface energy for various interface structures for given (T, P_{O_2}) combinations. The interface phase diagram is then obtained by identifying the most stable (i.e., minimum energy) interface as a function of T and P_{O_2}. In the following paragraphs, we discuss the interface phase diagram obtained using both Equations 11.26 and 11.27 as well as the impact of including $\Delta F^{v}_{\theta_O}$ and $\Delta F^{c}_{\theta_O}$.

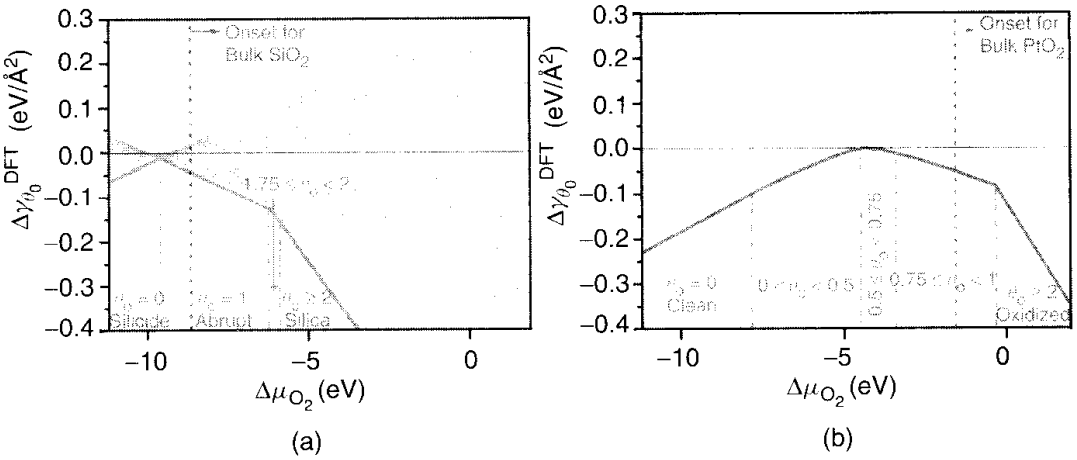

Figure 11.16 The relative interface free energy as a function of $\Delta\mu_{O_2}$ for the (a) Si-HfO_2 and (b) Pt-HfO_2 interfaces. The inner boundaries represent the lowest interface energy at each $\Delta\mu_{O_2}$ value. The corresponding θ_O value is indicated in the figure. The vertical dash-dotted lines are boundaries between two different stable interface structures. The onset $\Delta\mu_{O_2}$ to form bulk SiO_2 and α-PtO_2 is indicated by the vertical dotted line in (a) and (b), respectively [99]. (*See insert for color representation of the figure.*) (Reprinted with permission from H. Zhu, C. Tang, and R. Ramprasad, Phys Rev, 2010, B 82, 235413 and H. Zhu and R. Ramprasad, Phys. Rev,2011, B 83, 081416(R). Copyright 2010 by the American Physical Society.)

11.8.1 Interface Phase Diagrams Not Including Vibrational and Configurational Energies

We consider the interfaces first with the assumption that the contribution to the interface energy due to $\Delta F_{\theta_O}^{v}$ and $\Delta F_{\theta_O}^{c}$ may be ignored, as described by Equation 11.27. The advantage with considering Equation 11.27 is that all T and P_{O_2} dependence of $\Delta\gamma_{\theta_O}^{DFT}$ is contained solely within $\Delta\mu_{O_2}$. Thus, as shown in Figure 11.16, a plot of $\Delta\gamma_{\theta_O}^{DFT}$ versus $\Delta\mu_{O_2}$ yields straight lines, with the slope and intercept depending, respectively, on the interfacial O content and the value of $\Delta E_{\theta_O}^{DFT}$. The lower boundary of $\Delta\mu_{O_2}$ is confined to avoid the segregation of Hf from bulk HfO_2. Lines corresponding to each value of θ_O ranging from 0 to 2 are shown, and the lowest energy interface at each $\Delta\mu_{O_2}$ value is identified along with the corresponding θ_O value. The critical $\Delta\mu_{O_2}$ value, above which formation of the bulk XO_2 oxides occurs, is also indicated. At this critical $\Delta\mu_{O_2}$, bulk X is in equilibrium with bulk XO_2. The stable forms for bulk Hf, HfO_2, Pt, and PtO_2 are the hexagonal, monoclinic, face-centered cubic, and α-PtO_2 structures, respectively.

As shown in Figure 11.16a, the stable interface type in Si:θ_O:HfO_2 heterostructure changes abruptly from $\theta_O = 0$ to $\theta_O = 1$ and then to $\theta_O = 1.75$. Nevertheless, when $2 > \theta_O > 1.75$, the interface changes smoothly. Moreover, bulk SiO_2 is favored at smaller $\Delta\mu_{O_2}$ values than interfacial silica. This is probably due to the fact that the oxidation of interfacial silicon is accompanied by strain and

hence requires more energy. The Pt:θ_O:HfO_2 interface (shown in Fig. 11.16b), however, changes more smoothly for $\theta_O \leq 1$, and then abruptly changes from $\theta_O \sim 1$ to $\theta_O = 2$. Similar to the Si-HfO_2 case (and presumably for the same reason), the critical $\Delta\mu_{O_2}$ for an oxidized Pt-HfO_2 interface is larger than the one required to form bulk PtO_2.

Since $\Delta\mu_{O_2}$ is a function of T and P_{O_2}, the information contained in Figure 11.16 may be used to create (T, P_{O_2}) phase diagrams in which each $\Delta\mu_{O_2}$ "turning point" of Figure 11.16 becomes a curve in a T versus P_{O_2} plot, demarcating boundaries between two different phases. Such phase diagrams are presented in Figures 11.17a and Fig. 11.18a for Si-HfO_2 and Pt-HfO_2 interfaces, respectively, under the assumption that $\Delta F^{v}_{\theta_O}$ and $\Delta F^{c}_{\theta_O}$ may be ignored.

From Figure 11.17a, we find that (not surprisingly) the interfacial silica phase prefers high oxygen pressure and low temperature, while the silicide phase is stable at low oxygen pressure and high temperature. It is however interesting to note that interfacial silica can occur even at ultrahigh vacuum conditions ($P_{O_2} < 10^{-12}$ atm) in a wide temperature range, which explains why the interfacial silica phase is widely observed. The open and solid circles in Figure 11.17a, respectively, represent experimental conditions at which SiO_2 and SiO at Si-HfO_2 interfaces are known to occur [92, 93]. The gray filled circle stands for the critical point for interfacial SiO_2 to decompose to SiO [93]. The (T, P_{O_2}) boundaries predicted in Figure 11.17a for the decomposition of interfacial silica is consistent with experiments.

Compared to Si-HfO_2, the Pt-HfO_2 interface displays a smoother transition from one level of O coverage to another, especially for $\theta_O < 1$ (Fig. 11.18a). Also, this interface can be oxidized only at a very high oxygen pressure and low temperature. In the ultrahigh vacuum environment, the stable interfacial O coverage between Pt and HfO_2 is 0.5–1 ML. In view of the fact that experimental data for the Pt-HfO_2 interface morphologies is sparse, we compared our phase diagram with experimental data for Pt surface oxidation. In order to facilitate such a comparison, we make the following observation. Since 0.5 ML O at the Pt-HfO_2 interface passivates the dangling bonds on the HfO_2 side of the interface (based on the charge counting notions) and has little interaction with Pt, the net interfacial O strongly bonded to Pt is actually $\theta_O - 0.5$ ML. Within this context, the interfacial Pt in Pt:0.5:HfO_2 behaves like a clean Pt surface. The open and solid squares in Figure 11.18a stand for the (T, P_{O_2}) conditions at which 0.25 ML O-adsorbed (111) Pt and clean (111) Pt surfaces are observed in experiment, respectively, consistent with our $\theta_O - 0.5$ ML values of ~0.25 and 0, respectively, under those same conditions. Another interesting finding of this work is that the oxidation of Pt at the interface is similar to that of a free (111) Pt surface. The saturation coverage of the chemically adsorbed O on (111) Pt surface is 0.25–0.3 ML, after which a layer of PtO_2 forms immediately on the surface [104]. Here, we find that the corresponding $\theta_O - 0.5$ ML value beyond which interfacial PtO_2 is formed is 0.25–0.5.

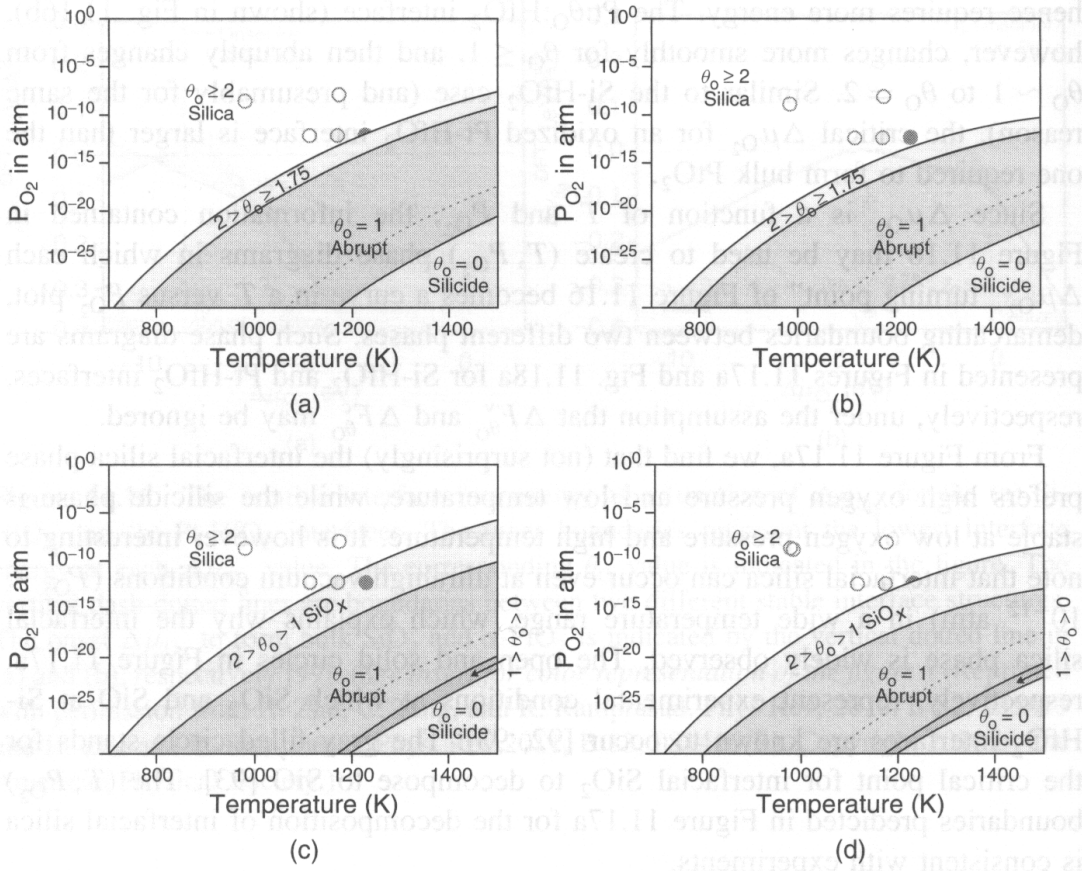

Figure 11.17 (a) The interface phase diagrams for the Si-HfO_2 interface, determined using Equation 11.27), *i.e.*, after neglecting the vibrational and configurational entropic contributions of the condensed phases to the relative interface free energy. (b) Same as (a), but with the vibrational entropic contribution ($\Delta F^{v}_{\theta_O}$) included. (c) Same as (a), but with the configurational entropic contribution ($\Delta F^{c}_{\theta_O}$) included. (d) The interface phase diagrams determined using Equation 11.26; this is the same as (a), but with both the vibrational and configurational entropic contributions included. The solid curves indicate the interface phase boundaries, and the dotted curves represent the onset of formation of bulk SiO_2. The open and solid circles stand for the condition to form SiO_2 and SiO at the Si-HfO_2 interfaces in experiments, respectively [92, 93]. The gray filled circle stands for the critical point for interfacial SiO_2 to decompose to SiO [93, 99]. (*See insert for color representation of the figure.*) (Reprinted with permission from H. Zhu, C. Tang, and R. Ramprasad, Phys Rev, 2010, B 82, 235413 and H. Zhu and R. Ramprasad, Phys. Rev,2011, B 83, 081416(R). Copyright 2010 by the American Physical Society.)

11.8.2 Impact of Other Factors (For Example, the Vibrational and Configurational Energy Contributions) on Interface Phase Diagrams

Next, we address theoretical aspects left unexplored in the treatment above, for example, the neglect of $\Delta F^{v}_{\theta_O}$ and $\Delta F^{c}_{\theta_O}$ (which allowed us to simplify Equation 11.26 to Equation 11.27]. To estimate $\Delta F^{v}_{\theta_O}$, the vibrational DOS, $\sigma_{\theta_O}(w)$, for an interface with a certain O coverage and frequency w have been determined

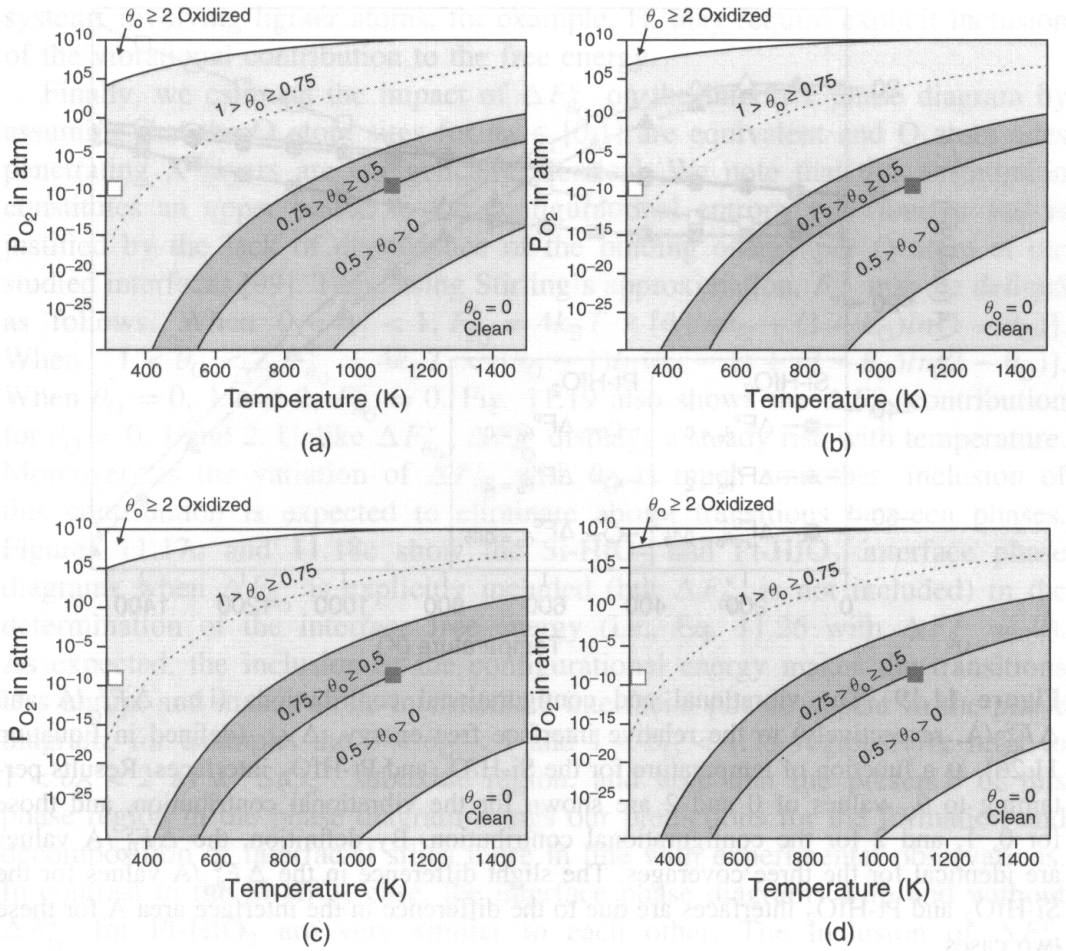

Figure 11.18 (a) The interface phase diagrams for the Pt-HfO_2 interface, determined using Equation 11.27, that is, after neglecting the vibrational and configurational entropic contributions of the condensed phases to the relative interface free energy. (b) Same as (a), but with the vibrational entropic contribution ($\Delta F^{v}_{\theta_O}$) included. (c) Same as (a), but with the configurational entropic contribution ($\Delta F^{c}_{\theta_O}$) included. (d) The interface phase diagrams determined using Equation 11.26; this is the same as (a), but with both the vibrational and configurational entropic contributions included. The solid curves indicate the interface phase boundaries, and the dotted curves represent the onset of formation of bulk PtO_2. The open and solid squares are the T and P_{O_2} when a 0.25 ML O-adsorbed (111) Pt surface and a clean (111) Pt surface were observed, respectively [99, 104]. (*See insert for color representation of the figure.*) (Reprinted with permission from H. Zhu, C. Tang, and R. Ramprasad, Phys Rev., 2010, B 82, 235413 and H. Zhu and R. Ramprasad, Phys. Rev., 2011, B 83, 081416(R). Copyright 2010 by the American Physical Society.)

through harmonic normal mode analysis by allowing only the interfacial O, Si, Pt, or Hf atoms, as appropriate, to vibrate. The vibrational contribution to the interface free energy (to be used in Equation 11.26), can be calculated by Equation 11.19. The vibration of atoms away from the interface for θ_O and 0.5 are expected to be roughly equivalent and are assumed to cancel out in the computation of $\Delta F^{v}_{\theta_O}$. For clarity, we show $\Delta F^{v}_{\theta_O}/A$ for θ_O values of only 0 and 2 in

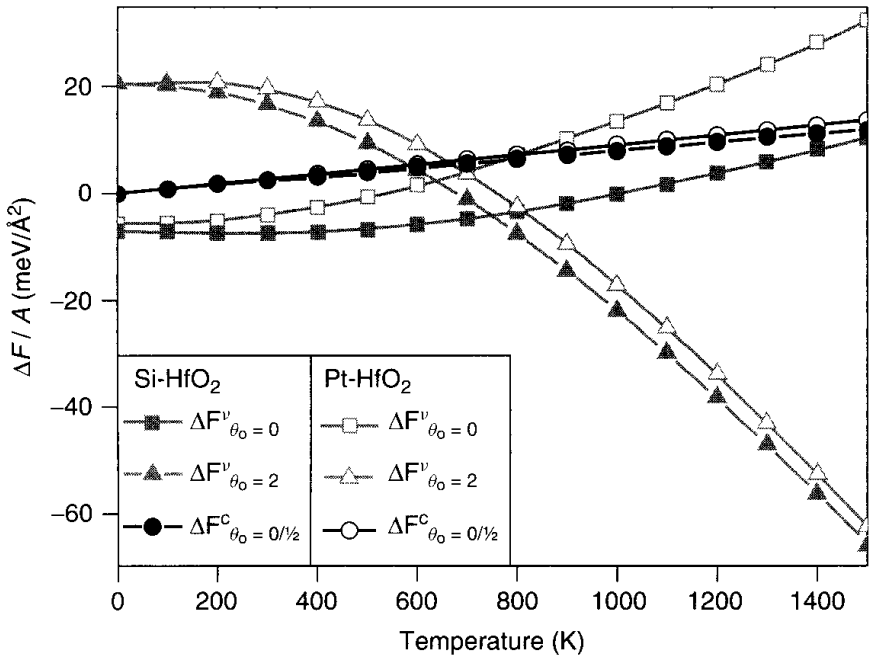

Figure 11.19 The vibrational and configurational contributions (i.e., $\Delta F^{v}_{\theta_O}$/A and $\Delta F^{c}_{\theta_O}$/A, respectively) to the relative interface free energy, $\Delta\gamma_{\theta_O}$ (defined in Equation 11.26], as a function of temperature for the Si-HfO_2 and Pt-HfO_2 interfaces. Results pertaining to θ_O values of 0 and 2 are shown for the vibrational contribution, and those for 0, 1, and 2 for the configurational contribution. By definition, the $\Delta F^{c}_{\theta_O}$/A values are identical for the three coverages. The slight difference in the $\Delta F^{c}_{\theta_O}$/A values for the Si-HfO_2 and Pt-HfO_2 interfaces are due to the difference in the interface area A for these two cases.

Figure 11.19 as these two extreme coverages provide an idea of the magnitude of the vibrational energy contribution. The roughly flat region at low temperatures is due to zero point vibrations (first term of Equation 11.19]. The temperature-dependent (second) term of Equation 11.19 contributes to a decrease (increase) of $\Delta F^{v}_{\theta_O}$ with increasing temperature for θ_O values larger (smaller) than 0.5, and in all cases going through zero above 500 K. This has the implication that lower (higher) values of the O coverages are favored at lower (higher) temperatures, with the vibrational entropic contribution having negligible impact in an intermediate temperature range when $\Delta F^{v}_{\theta_O}$ goes through zero. Features that reflect these expectations indeed manifest in the phase diagrams of Figures 11.17b and 11.18b, which have been created for the Si-HfO_2 and Pt-HfO_2 interfaces with the explicit inclusion of $\Delta F^{v}_{\theta_O}$ in the determination of the interface free energy (that is, Eq. 11.26 with $\Delta F^{c}_{\theta_O} = 0$). It can be seen that the impact of including $\Delta F^{v}_{\theta_O}$ results in rather minor changes to the features of the phase diagrams (most notably, the enlargement of the $\theta_O \geq 2$ phase region at high temperatures in the Si-HfO_2 interface phase diagram, and a shrinking of this region in the Pt-HfO_2 interface phase diagram at low temperatures). While this analysis provides a justification for the neglect of the vibrational contribution in prior treatments, we note that

systems involving lighter atoms, for example, H, may require explicit inclusion of the vibrational contribution to the free energy.

Finally, we estimate the impact of $\Delta F^{c}_{\theta_O}$ on the interface phase diagram by assuming that the O atom sites for $\theta_O \in [0,1]$ are equivalent and O atom sites penetrating X layers are energetically identical. We note that this assumption constitutes an upper bound to the configurational entropy contribution and is justified by the lack of dependence of the binding energy per O atom at the studied interfaces [99]. Thus, using Stirling's approximation, $F^{c}_{\theta_O}$ may be defined as follows. When $0 < \theta_O < 1$, $F^{c}_{\theta_O} = 4k_BT \times [\theta_O ln\theta_O + (1-\theta_O)ln(1-\theta_O)]$. When $1 < \theta_O < 2$, $F^{c}_{\theta_O} = 4k_BT \times [(\theta_O - 1)ln(\theta_O - 1) + (2-\theta_O)ln(2-\theta_O)]$. When $\theta_O = 0$, 1 and 2, $F^{c}_{\theta_O} = 0$. Fig. 11.19 also shows the $\Delta F^{c}_{\theta_O}$ contribution for $\theta_O = 0$, 1 and 2. Unlike $\Delta F^{v}_{\theta_O}$, $\Delta F^{c}_{\theta_O}$ displays a steady rise with temperature. Moreover, as the variation of $\Delta F^{c}_{\theta_O}$ with θ_O is much smoother, inclusion of this contribution is expected to eliminate abrupt transitions between phases. Figures 11.17c and 11.18c show the Si-HfO_2 and Pt-HfO_2 interface phase diagrams when $\Delta F^{c}_{\theta_O}$ is explicitly included (but $\Delta F^{v}_{\theta_O}$ is not included) in the determination of the interface free energy (i.e., Eq. 11.26 with $\Delta F^{v}_{\theta_O} = 0$). As expected, the inclusion of the configurational energy makes the transitions less abrupt and makes some intermediate interfacial phases appear in the phase diagram, for example, the $0 < \theta_O < 1$ and $1 < \theta_O < 1.75$ regions. We refer to $1 < \theta_O < 2$ as a "SiO_x" suboxide region, and note that the presence of this phase region in the phase diagram brings our predictions for the formation and decomposition of interfacial silica more in line with experimental observations. In contrast to the Si-HfO_2 case, the interface phase diagrams with and without $\Delta F^{c}_{\theta_O}$ for Pt-HfO_2 are very similar to each other. The inclusion of $\Delta F^{c}_{\theta_O}$ causes only slight shifts to the phase boundaries, and no new phase regions appear.

Figures 11.17d and 11.18d display the corresponding phase diagrams when both the vibrational and configurational energies are included in the treatment (i.e., when Equation 11.26 is used]. Not surprisingly, simultaneous inclusion of these two contributions also does not result in significant differences with respect to the phase diagrams of Figures 11.17a and 11.18a. Nevertheless, these calculations provide an estimate of errors that may be introduced due to the neglect of such contributions.

We note that the obtained phase diagrams are in agreement with available experimental data. While such an agreement with experiments may be viewed as fortuitous, this may indicate that all the dominant contributions to the interface free energy have been included in this treatment (even at the level of Equation 11.27). The unaddressed issues of deficiencies inherent to approximations within DFT are presumably unimportant in the class of systems studied here (or may have participated in a fortuitous cancelation of errors). We do note that FPT studies may benefit from (the relatively inexpensive) explicit inclusion of configurational entropic contributions to the free energy, especially when a lack of such inclusion results in abrupt transitions between phases.

11.9 OUTLOOK AND CONCLUDING THOUGHTS

This article focused on the practical applications of modern DFT-based computations in the area of surface and interface science. After a general survey of the current state-of-the-art of conventional DFT computations, applications of such methods to the computations of surface energies, optimization of nanostructure shapes, and the determinations of surface and interface phase diagrams were explored. Methods for combining traditional zero-temperature DFT results with statistical mechanics to obtain free energies of processes were also described.

The future prospects for DFT-based computations remains exciting. The spectrum of problems that may be addressed using DFT methods is rapidly increasing. Moreover, methods to deal with some of the remaining fundamental deficiencies of DFT—such as predictions of band gaps and gap levels in insulators [105] and the treatment of secondary bonding interactions (e.g., dispersive van der Waals interactions) [106]—are becoming available and practical. As we go to more extreme conditions, such as high temperatures and pressures, the free energy of the system has to include terms beyond the harmonic approximation (for the vibrational part). Robust schemes for the proper treatment of such factors are also beginning to mature [107]. The technologically important topic of surface/interface science will benefit from these recent and anticipated developments.

ACKNOWLEDGMENTS

The authors acknowledge support of their surface/interface research by the National Science Foundation, the Office of Naval Research, the ACS Petroleum Research Fund, the Department of Energy, and the Alexander von Humboldt Foundation.

REFERENCES

1. Somorjai GA. *Introduction to Surface Chemistry and Catalysis*. New York: John Wiley and Sons, Inc.; 1994.
2. Woodruff DP, Delchar TA. *Modern Techniques of Surface Science*. 2nd ed. Cambridge: Cambridge University Press; 1994.
3. Noguera C. *Physics and Chemistry of Oxide Surfaces*. New York: Cambridge University Press; 1996.
4. Groß A. *Theoretical Surface Science A Microscopic Perspective*. Berlin: Springer; 2002.
5. Kolasinski KW. *Surface Science: Foundations of Catalysis and Nanoscience*. England: John Wiley and Sons, Ltd; 2008. Yip S, editor. *Handbook of Materials Modeling*. Berlin: Springer; 2005.
6. Horn K, Scheffler M, editors. Volume 2, *Handbook of Surface Science: Electronic Structure*. Amsterdam: Elsevier; 2000.

7. Chadi DJ. Phys Rev Lett 1979;43:43.
8. Brink RS, Verwoerd WS. Surf Sci 1981;154:L203.
9. Ihm J, Cohen ML, Chadi DJ. Phys Rev B 1980;21:4592.
10. Yin MT, Cohen ML. Phys Rev B 1981;24:2303.
11. Verwoerd WS. Surf Sci 1981;99:581.
12. Krüger E, Pollmann J. Phys Rev B 1988;38:10578.
13. Brommer KD, Needels M, Larson BE, Joannopoulos JD. Phys Rev Lett 1992; 68:1355.
14. Stich I, Payne MC, King-Smith RD, Lin J-S. Phys Rev Lett 1992;68:1351.
15. Sholl DS, Steckel JA. *Density Functional Theory: A Practical Introduction*. New Jersey: John Wiley and Sons, Inc.; 2009.
16. Honkala K, Hellman A, Remediakis IN, Logadottir A, Carlsson A, Dahl S, Christensen CH, Nøskov JK. Science 2005;307:555.
17. Rieger M, Rogal J, Reuter K. Phys Rev Lett 2008;100:016105. C Stampfl, M Schemer, Surf. Sci., 319, L23 (1994).
18. Burchhardt J, Nielsen MM, Adams DL, Lundgren E, Andersen JN, Stampfl C, Scheffler M, Schmalz A, Aminpirooz S, Haase J. Phys Rev Lett 1995;74:1617.
19. Stampfl C, Kreuzer HJ, Payne SH, Pfnür H, Scheffler M. Phys Rev Lett 1999; 83:2993.
20. Stampfl C, Kreuzer HJ, Payne SH, Scheffler M. Appl Phys A 1999;69:471.
21. Reuter K, Stampfl C, Scheffler M. In: Yip S, editor. Volume 1, *Handbook of Materials Modeling*. Berlin: Springer; 2005. p 149–194.
22. Hohenberg P, Kohn W. Phys Rev 1964;136:B864.
23. Kohn W, Sham L. Phys Rev 1965;140:A1133.
24. Parr RG, Yang W. *Density Functional Theory of Atoms and Molecules*. New York: Oxford University Press; 1989.
25. Dreizler RM, Gross EKU. *Density Functional Theory*. Berlin: Springer; 1990.
26. Martin R. *Electronic Structure: Basic Theory and Practical Methods*. New York: Cambridge University Press; 2004.
27. Kobayyashi K. Surf Sci 2001;493:665.
28. Kamran S, Chen K, Chen L. Phys Rev B 2009;79:024106.
29. Sun G, Kurti J, Rajczy P, Kertesz M, Hafner J, Kresse G. J Mol Struct (Theochem) 2003;624:37.
30. Ramprasad R, Shi N, Tang C. Modeling the physics and chemistry of interfaces in nanodielectrics. In: Nelson JK, editor. *Dielectric Polymer Nanocomposites*. New York: Springer; 2010.
31. Bernardini F, Fiorentini V. Phys Rev B 1998;58:15292.
32. Beche AD. Phys Rev A 1986;33:2756.
33. Robertson J, Xiong K, Clark SJ. Thin Solid Films 2006;496:1.
34. Shishkin M, Marsman M, Kresse G. Phys Rev Lett 2007;99:246403.
35. Ramprasad R, Classford KM, Adams JB, Masel RI. Surf Sci 1996;360:31.
36. Krukau AV, Vydrov OA, Izmaylov AF, Scuseria GE. J Chem Phys 2006;125: 224106.
37. Mitas L, Martin RM. Phys Rev Lett 1994;72:2438.

38. Vitos L, Ruban AV, Skriver HL, Kollar J. Surf Sci 1998;411:186.
39. Goniakowski J, Finocchi F, Noguera C. Rep Prog Phys 2008;71:016501.
40. Pashley MD. Phys Rev B 1989;40:10481.
41. Peng ZA, Peng XJ. J Am Chem Soc 2002;124:3343.
42. Zhang SB, Wei SH. Phys Rev Lett 2004;92(8):086102.
43. Manna L, Wang LW, Cingolani R, Alivisatos AP. J Phys Chem B 2005;109(13): 6183.
44. Pilania G, Sadowski T, Ramprasad R. J Phys Chem C 2009;113:1863.
45. Wulff G. Z Kristallogr 1901;34:449.
46. Herring C. Phys Rev 1951;82:87.
47. Shi H, Stampfl C. Phys Rev B 2008;77:094127.
48. Hu J, Li L, Yang W, Manna L, Wang L, Alivisatos AP. Science 2001;292:2060.
49. Chen X, Nazzal A, Goorskey D, Xiao M, Peng ZA, Peng X. Phys Rev B 2001; 64:245304.
50. Huynh WU, Dittmer JJ, Alivsatos AP. Science 2002;295:2425.
51. Carbone L, Nobile C, De Giorgo M, Sala FD, Morello G, Pompa P, Hytch M, Snoeck E, Fiore A, Franchini IR, Nadasan M, Silvestre AF, Chiodo L, Kudera S, Cingolani R, Krahne R, Manna L. Nano Lett 2007;7(10):2942.
52. Talapin DV, Koeppe R, Götzínger S, Kornowski A, Lupton JM, Rogach AL, Benson O, Feldmann J, Weller H. Nano Lett 2003;3(12):1677.
53. Mokari T, Rothenberg E, Popov I, Costi R, Banin U. Science 2004;304:1787.
54. Sheldon MT, Trudeau PE, Mokari T, Wang LW, Alivisatos AP. Nano Lett 2009; 9:3676.
55. Doll JD, Pilania G, Ramprasad R, Papadimitrakopoulos F. Nano Lett 2010;10:680.
56. Li R, Luo Z, Papadimitrakopoulos FJ. J Am Chem Soc 2006;128:6280.
57. Anpo M, Che M. Adv Catal 1999;44:119.
58. Hacquart R, Krafft JM, Costentin G, Jupille J. Surf Sci 2005;595:172.
59. Giordano L, Goniakowski J, Suzanne J. Phys Rev Lett 1998;81:1271.
60. Odelius M. Phys Rev Lett 1999;82:3919.
61. Delle Site L, Alavi A, Lynden-Bell RM. J Chem Phys 2000;113:3344.
62. Giordano L, Goniakowski J, Suzanne J. Phys Rev B 2000;62:15406.
63. Kim YD, Stultz J, Goodman DW. J Phys Chem B 2002;106:1515.
64. Stirniman MJ, Huang C, Smith RS, Joyce SA, Kay BD. J Chem Phys 1996;105: 1295.
65. Liu P, Kendelewicz T, Brown GJr., ParksGA. Surf Sci 1998;412:287.
66. Liu P, Kendelewicz T, Brown GJr., ParksGA. Surf Sci 1998;412:315.
67. Abriou D, Jupille J. Surf Sci 1999;430:L527.
68. Ahmed SI, Perry S, El-Bjeirami O. J Phys Chem B 2000;104:3343.
69. Scamehorn CA, Harrison NM, McCarthy MI. J Chem Phys 1994;101:1547.
70. Goniakowski J, Noguera C. Surf Sci 1995;330:337.
71. Langel W, Parrinello M. J Chem Phys 1995;103:8.
72. Refson K, Wogelius RA, Fraser DG, Payne MC, Lee MH, Milman V. Phys Rev B 1995;52:10823.

73. de Leeuw NH, Watson GW, Parker SC. J Chem Phys 1995;99:17219.
74. Mejias JA, Berry AJ, Refson K, Fraser DG. Chem Phys Lett 1999;314:558.
75. Finocchi F, Goniakowski J. Phys Rev B 2001;64:125426.
76. Ealet B, Goniakowski J, Finocchi F. Phys Rev B 2004;69:054419.
77. Costa D, Chizallet C, Ealet B, Goniakowski J, Finocchi F. J Chem Phys 2006;125:054702.
78. Finocchi F, Goniakowski J. Surf Sci 2007;601:4144.
79. Zhong Y, Zhu H, Shaw LL, Ramprasad R. Acta Mater 2011;59:3748–3757.
80. Jack DH. In: Schwartz MM, editor. *Engineering Application of Ceramic Materials: Source Book*. Materials Park (OH): American Society for Metals; 1985. p 147–153.
81. Exner HE. Int Met Rev 1979;24:149.
82. Kim CS, Rohrer GS. Interface Sci 2004;12:19.
83. Suetin DV, Shein IR, Kurlov AS, Gusev AI, Ivanovski AL. Phys Solid State 2008;50:1420.
84. Hammer B, Nørskov JK. Adv Catal 2000;45:71.
85. Newns DM. Phys Rev 1969;178:1123.
86. Anderson PW. Phys Rev 1961;124:41.
87. Hammer B, Nørskov JK. In: Lambert R, Pacchioni G, editors. *Theory of Adsorption and Surface Reactions*, NATO ASI Series E 331. Dordrecht: Kluwer Academic Publishers; 1997. K Reuter, M Scheffler, Phys. Rev. Lett., 90, 046103 (2003). RB Getman, WF Schneider, AD Smeltz, WN Delgass, FH Ribeiro, Phys. Rev. Lett., 102, 076101 (2009). R Grau-Crespo, KC Smith, TS Fisher, NH de Leeuw, UV Waghmare, Phys. Rev. B, 80, 174117 (2009). CG Van de Walle, J Neugebauer, Phys. Rev. Lett., 88, 066103 (2002).
88. Wallace RM, Wilk GD. Crit Rev Solid State Mater Sci 2003;28:231.
89. Wu M, Alivov YI, Morkoc H. J Mater Sci Mater Electron 2008;19:915.
90. Qiu XY, Liu HW, Fang F, Ha MJ, Liu JM. Appl Phys Lett 2006;88:072906.
91. Preisler EJ, Guha S, Copel M, Bojarczuk NA, Reuter MC, Gusev E. Appl Phys Lett 2004;85:6230.
92. (a) Wang SJ, Lim PC, Huan ACH, Liu CL, Chai JW, Chow SY, Pan JS. Appl Phys Lett 2003;82:2047; (b) Copel M, Reuter MC, Jamison P. Appl Phys Lett 2004;85:458.
93. Miyata N, Nabatame T, Horikawa T, Ichikawa M, Toriumi A. Appl Phys Lett 2003;82:3880.
94. Cho D-Y, Park K-S, Choi B-H, Oh S-J, Chang YJ, Kim DH, Noh TW, Jung R, Lee J-C. Appl Phys Lett 2005;86:041913.
95. Peacock PW, Robertson J. Phys Rev Lett 2004;92:057601.
96. Tang C, Tuttle B, Ramprasad R. Phy Rev B 2007;76:073306.
97. Tang C, Ramprasad R. Phy Rev B 2007;75:241302(R).
98. Tang C, Ramprasad R. Appl Phys Lett 2008;92:182908.
99. (a) Zhu H, Tang C, Ramprasad R. Phys Rev B 2010;82:235413; (b) Zhu H, Ramprasad R. Phys Rev B 2011;83:081416(R).
100. Stull DR, Prophet H. *JANAF Thermochemical Tables*. 2nd ed. Washington (DC): U.S. National Bureau of Standards; 1971.

101. (a) Hill TL. *Introduction to Statistical Thermodynamics*. New York: Dover; 1986; (b) Nash LK. *Elements of Statistical Thermodynamics*. Reading (MA): Addison-Wesley; 1972.
102. Reuter K, Scheffler M. Phys Rev B 2001;65:035406.
103. Reuter K, Scheffler M. Phys Rev B 2003;68:045407.
104. Engstrom U, Ryberg R. Phys Rev Lett 1999;82:2741.
105. Lambrecht WRL. Phys Status Solidi B, 1–12 (2010).
106. Grimme S. Wiley Interdisciplinary Rev: Comput Mol Sci 2011;1:211.
107. Grabowski B, Ismer L, Hickel T, Neugebauer J. Phys Rev B 2009;79:134106.